

STRUCTURED RED GIANT WINDS WITH MAGNETIZED HOT BUBBLES AND THE CORONA/COOL WIND DIVIDING LINE

TAKERU K. SUZUKI¹
Submitted to ApJ

ABSTRACT

By performing magnetohydrodynamical (MHD) simulations, we investigate the mass loss of intermediate- and low-mass stars from main sequence (MS) to red giant branch (RGB) phases. Alfvén waves, which are excited by the surface convections travel outwardly and dissipate by nonlinear processes to accelerate and heat the stellar winds. We dynamically treat these processes in open magnetic field regions from the photospheres to $\simeq 25$ stellar radii. When the stars evolve to slightly blueward positions of the dividing line (Linsky & Haisch), the steady hot corona with temperature, $T \approx 10^6$ K, suddenly disappears. Instead, many hot ($\sim 10^6$ K) and warm ($\gtrsim 10^5$ K) bubbles are formed in cool ($T \lesssim 2 \times 10^4$ K) chromospheric winds because of thermal instability; the red giant wind is not a steady stream but structured outflow. As a result, the mass loss rates, \dot{M} , largely vary in time by 3-4 orders or magnitude in the RGB stars. Supported by magnetic pressure, the density of hot bubbles can be kept low to reduce the radiative cooling and to maintain the high temperature long time. Even in the stars redward of the dividing line, hot bubbles intermittently exist, and they can be sources of ultraviolet/soft X-ray emissions from hybrid stars. Nearly static regions are formed above the photospheres of the RGB stars, and the stellar winds are effectively accelerated from several stellar radii. Then, the wind velocity is much smaller than the surface escape speed, because it is regulated by the slower escape speed at that location. We finally derive an equation that determines \dot{M} from the energetics of the simulated wave-driven winds in a *forward* manner. The relation explains \dot{M} from MS to RGB, and it can play a complementary role to the Reimers' formula, which is mainly for more luminous giants.

Subject headings: magnetic fields – stars: coronae – stars: late type – stars: mass loss – stars: winds, outflows – waves

1. INTRODUCTION

Solar-type stars have X-ray emitting coronae with the temperatures, $T \gtrsim 10^6$ K, and hot stellar winds stream out with the asymptotic terminal velocities, $v_\infty = 100 - 1000$ km s⁻¹, comparable to the escape velocities at the surfaces. The total mass lost by the wind is negligible during the main sequence (MS) phase in comparison with the stellar mass, whereas the wind may play a role in the loss of the angular momentums. Along with the stellar evolution to red giant branch (RGB), the mass loss rate, \dot{M} 's, increases by 4-10 orders of magnitude (Judge & Stencel 1991), while v_∞ drops to 10–100 km s⁻¹, which is smaller than the surface escape velocity. In addition, the temperature of the wind also decreases, which is probably drastic across the “dividing line” (DL hereafter; Linsky & Haisch 1979) discussed below. The mass loss during the RGB phase becomes more important, and it may control the later evolution of a star itself. For instance, some stars evolve to a peculiar group of blue horizontal branch stars, and it is inferred that it is related to the mass loss during the RGB phase (Yi, Demarque, & Kim 1997). In spite of its importance, however, the acceleration mechanism of red giant winds is not well understood.

It was reported that cool single RGB stars redward of the DL (near spectral type K1 III in Hertzsprung-

Russel (HR)-diagram; Figure 1) showed an evidence of neither ultraviolet (UV) radiation of C_{IV} ($T \sim 10^5$ K) (Linsky & Haisch 1979) nor soft X-ray ($T \sim 10^6$ K) (Ayres et al. 1981). Stencel & Mullan (1980) further pointed out that the stellar winds appear cool and massive after stars cross the DL. However, Hartmann, Dupree, & Raymond (1980) observed late-type super-giants in the noncoronal zone that exhibit both UV emission and blue-shifted chromospheric absorption features, indicating that hot gas and cool outflow coexist. Such hybrid stars were also detected by later observations (e.g. Ayres et al. 1998), whereas the activity levels of UV/soft X-ray are much lower than in the coronal zone. These observations show that the simple DL picture roughly holds while the reality seems a bit more complicated.

RGB stars are generally slow rotators. The radiation luminosities of intermediate- and low-mass stars near the DL are not still large, either. Therefore, the centrifugal force and radiation pressure are not sufficient in accelerating the stellar winds (e.g. Judge & Stencel 1991). Instead, the surface convective layer is expected to be the main origin of driving the winds and UV/X-ray activities. Magnetic fields are probably generated by turbulent dynamo in the convection zone. The energy of the surface turbulences is lifted up through the magnetic fields, and the dissipation of the energy in upper regions leads to the heating of the atmosphere and the acceleration of the wind. This picture is essentially the same as what takes place in the solar corona and wind. Difference

Electronic address: stakeru@ea.c.u-tokyo.ac.jp

¹School of Arts and Sciences, University of Tokyo, Komaba, Meguro, Tokyo, Japan 153-8902

from the sun is that the surface gravity is much smaller in RGB stars. In a naïve way of thinking, the transition from the steady coronae to the cool winds (with some hybrid activities) is possibly explained by this gravity effect even though other conditions are similar; the cool atmosphere comes to flow out before heated up to coronal temperature ($T \sim 10^6$ K), as the gravity confinement weakens.

Many pioneering works have tried to reveal nature of red giant winds (e.g. Hartmann & MacGregor 1980; Holzer, Flå, & Leer 1983; Charboneau & MacGregor 1995). However, the consecutive processes from the surface to the wind explained above have not been studied self-consistently; previous model calculations started from locations far above the photosphere in order to avoid difficulties arising from the huge density contrast. Moreover, they assume mechanical or phenomenological “wave” energies with somewhat ad hoc prescription of the dissipation.

In this paper, we perform dynamical simulations of stellar winds from the photosphere to $\simeq 25 R_*$ in open magnetic field regions, where R_* is stellar radius. We give perturbations at the photosphere originating from the surface convection. These fluctuations excite waves that propagate upwardly. Among various modes the Alfvén wave travels to a sufficiently large distance to contribute to the acceleration and heating of the stellar wind. We simulate the propagation and dissipation of the waves by solving nonlinear MHD equations, and treat the heating and acceleration of the gas in a fully self-consistent manner without conventional heating functions (§3.4.2). Wind properties, such as \dot{M} and v_∞ , are determined from the surface conditions without ad hoc parameters. Another advantage of dynamical simulations is that we do not have to care about the critical (sonic) point(s), which is often problematic when constructing a transonic wind solution under the steady-state condition. A stable wind structure is automatically selected whether it is transonic or subsonic.

We already carried out simulations in the solar corona and wind (Suzuki & Inutsuka 2005, 2006, hereafter SI05; SI06). We showed that the coronal heating and solar wind acceleration in the open field regions are natural consequences of the photospheric perturbations; the Alfvén waves generated from the surface effectively dissipate in the corona by nonlinear mechanism to sufficiently heat and accelerate the solar wind in spite of the energy loss via radiative cooling, thermal conduction, and wave reflection. The aim of this paper is to study the evolution of the stellar winds from MS to RGB stages by extending this work to cool RGB stars. We investigate the stellar winds of a $1M_\odot$ star from MS (*i.e.* present sun) to RGB across the DL, where M_\odot is the solar mass. For comparison we also study a more massive RGB star with $3M_\odot$ both blueward and redward of the DL.

§2 presents our simulation method. In §3 we show the results of the simulations, focusing on the evolution and time-dependent nature of the stellar winds. We discuss comparisons with related works as well as the uncertainties and limitations of our simulations in §4.

2. SIMULATION SET-UP

2.1. Simulated Stars

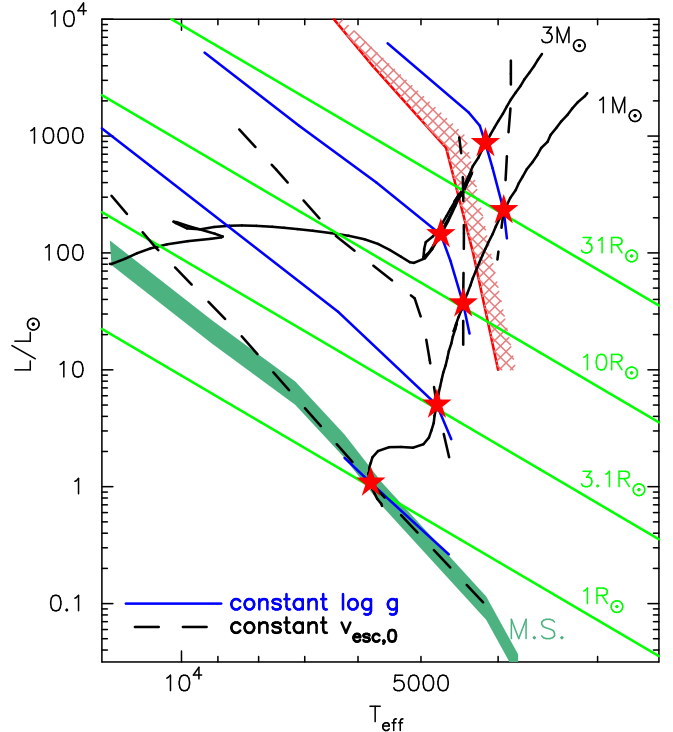


FIG. 1.— Simulated stars in HR-diagram. The six red stars correspond to Models tabulated in Table 1. The black solid lines are the evolutionary paths of $1 M_\odot$ and $3 M_\odot$ stars with the solar abundance (Girardi et al. 2000). The red line with the cross hatch is the DL (Linsky & Haisch 1979). The green solid lines indicate constant stellar radii, $R_* = 1 R_\odot$, $3.1 R_\odot$, $10 R_\odot$, and $31 R_\odot$ from below. The blue lines indicate constant gravity, $\log g = 4.4$, 3.4 , 2.4 , 1.4 from below. The black dashed lines indicate constant escape speeds from the stellar surfaces, $v_{\text{esc},0} = 617$, 347 , 195 , 110 km s $^{-1}$ from below. The dark green shaded region denotes the location of main sequence stars.

We simulate the Alfvén wave-driven stellar winds of the various stars summarized in Table 1 and in Figure 1. First, we consider the $1 M_\odot$ stars with different stellar radii, $R_* = 1 R_\odot$ (*i.e.* the present sun), $3.1 R_\odot$, $10 R_\odot$, and $31 R_\odot$, where R_\odot is solar radius, to study the evolution of the winds; note that the DL is between the latter two cases. We also simulate the stars with $3M_\odot$ near the DL to compare with the $1 M_\odot$ cases. Here we adopt the stellar evolutionary tracks from Girardi et al. (2000) to determine the basic stellar parameters, such as R_* and effective temperatures, T_{eff} , which are used to estimate the densities, ρ_0 , at the photospheres and the photospheric amplitudes, δv_0 , of the surface convection (§2.3).

2.2. Simulation Details

We consider 1D flux tubes that are super-radially open. As shown in Figure 2, a certain fraction of the stellar surface is covered by closed loops so that open flux tubes diverge more rapidly than the radial expansion (Kopp & Holzer 1976).

We inject velocity and magnetic field fluctuations originating from the surface convection at the photospheres, which are the inner boundaries of the simulations (§2.3). These fluctuations excite various waves, a fraction of which propagate upwardly. We treat both energy and

Model	$M_\star(M_\odot)$	$R_\star(R_\odot)$	$T_{\text{eff}}(\text{K})$	$\log g$	$v_{\text{esc},0}(\text{km s}^{-1})$	$\rho_0(\text{g cm}^{-3})$	$\langle\delta v_0\rangle(\text{km s}^{-1})$	$\tau_{\text{min}}(\text{min})$	$\tau_{\text{max}}(\text{min})$	$R_1(R_\star)$	$R_2(R_\star)$
I	1	1	5800	4.4	617	1.0×10^{-7}	1.0	1	32	1.01	1.2
II	1	3.1	4800	3.4	347	5×10^{-8}	1.5	9	290	1.031	1.4
III	1	10	4500	2.4	195	1.5×10^{-8}	2.8	87	2800	1.1	1.5
IV	1	31	3900	1.4	110	4.5×10^{-9}	5.3	800	25600	1.31	1.8
V	3	17.3	4700	2.4	255	1.5×10^{-8}	3.7	90	2900	1.1	1.5
VI	3	54.8	4200	1.4	144	4×10^{-9}	8.0	930	29900	1.31	1.8

TABLE 1

MODEL PROPERTIES. TABULATED FROM LEFT TO RIGHT ARE RESPECTIVELY STELLAR MASS, M_\star , IN M_\odot , STELLAR RADIUS, R_\star , IN R_\odot , EFFECTIVE TEMPERATURE, T_{eff} (K), LOGARITHM OF SURFACE GRAVITY, $g = GM_\star/R_\star^2$, ESCAPE SPEED AT THE SURFACE, $v_{\text{esc},0} \equiv v_{\text{esc}}(R_\star) = \sqrt{2GM_\star/R_\star}$, PHOTOSPHERIC DENSITY, $\rho_0(\text{G CM}^{-3})$, ROOT-MEAN-SQUARED AMPLITUDE OF TRANSVERSE FLUCTUATION AT THE PHOTOSPHERE, $\langle\delta v_0\rangle$ (KM S $^{-1}$), MINIMUM WAVE PERIOD, τ_{min} , MAXIMUM WAVE PERIOD, τ_{max} , AND LOCATIONS OF FLUX TUBE EXPANSIONS, R_1 AND R_2 .

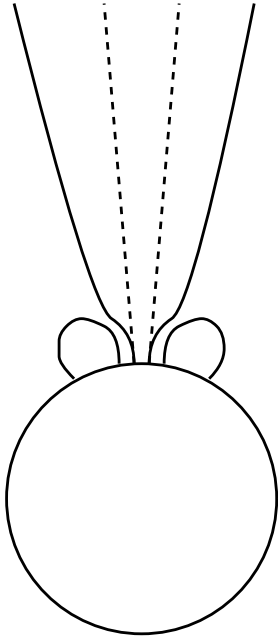


FIG. 2.— Schematic picture of a magnetic flux tube that is super-radially open. The solid lines denote magnetic field lines. The open field region expands more rapidly than the spherical expansion shown by the dashed lines. Our simulations treat such super-radially open flux tubes.

momentum transfers in stellar winds, namely the propagation and dissipation of the waves and the consequent acceleration and heating of the surrounding gas, in a self-consistent manner. We set the outer boundaries at $\simeq 25 R_\star$ at which the outgoing condition of both materials and MHD waves is properly prescribed (SI06). In this paper we neglect centrifugal force, which is a reasonable assumption since low mass MS stars and RGB stars generally rotate slowly, and radiation pressure, which is also appropriate, where it might become important in more evolved asymptotic giant branch stars with dusts in the atmospheres.

Radial field strength, B_r , is given by the conservation of magnetic flux as

$$B_r r^2 f(r) = \text{const.}, \quad (1)$$

where $f(r)$ is a super-radial expansion factor. A 1D flux tube is fixed by the field strength at the photosphere, $B_{r,0}$, and $f(r)$. We set $B_{r,0}$ and $f(r)$ based on our previous solar studies (SI05; SI06). While the average field

strength is 1 – 10 G on the solar photosphere, magnetic field lines are swept into inter-granulation lanes so that the localized strength becomes $\gtrsim 100$ G to a few kG. These field lines rapidly expand and becomes $\lesssim 10$ G in the coronal region. Finally in the outer region (\gtrsim a few R_\star) the field lines distribute almost radially.

We use the same $B_{r,0} = 240$ G and the same total expansion factor, $f_{\text{tot}} = 240$, for all the Models. Note that these values give $B_{r,0}/f_{\text{tot}} = 1$ G, which is the total magnetic flux of the open field regions divided by the stellar surface. The average field strength becomes larger by adding the contributions from closed field regions (§4.1). We use the same functional form of the expansion as in SI06 (see also Kopp & Holzer 1976):

$$f(r) = \frac{f_{1,\text{tot}} \exp\left(\frac{r-R_1}{\sigma_1}\right) + f_1}{\exp\left(\frac{r-R_1}{\sigma_1}\right) + 1} \frac{f_{2,\text{tot}} \exp\left(\frac{r-R_2}{\sigma_2}\right) + f_2}{\exp\left(\frac{r-R_2}{\sigma_2}\right) + 1} \quad (2)$$

where $f_1 = 1 - (f_{1,\text{tot}} - 1) \exp\left(\frac{R_\star - R_1}{\sigma_1}\right)$ and $f_2 = 1 - (f_{2,\text{tot}} - 1) \exp\left(\frac{R_\star - R_2}{\sigma_2}\right)$. A flux tube initially expands by a factor of $f_{1,\text{tot}}$ around $R_1 - \sigma_1 \sim R_1 + \sigma_1$, corresponding to the ‘funnel’ structure (Tu et al. 2005) by closed loops, and followed by $f_{2,\text{tot}}$ times expansion around $R_2 - \sigma_2 \sim R_1 + \sigma_2$ due to the large scale (dipole) magnetic fields. The total super-radial expansion is defined as $f_{\text{tot}} = f_{1,\text{tot}} f_{2,\text{tot}}$. We adopt $f_{1,\text{tot}} = 40$ and $f_{2,\text{tot}} = 6$ in all the Models. R_1 and R_2 of each Model are summarized in Table 1. $R_1 - R_\star$ is set to be (roughly) proportional to the scale height ($\propto g^{-1} = (GM_\star/R_\star^2)^{-1}$; see Equation 15 for a more specific form) because closed loops are supposed to be taller in lower gravity stars if the surface magnetic field conditions are the same (but see §4.1). Accordingly R_2 is also set to be larger in more evolved stars. We adopt the ‘widths’ of the expansions, $\sigma_1 \approx 0.6(R_1 - R_\star)$ and $\sigma_2 \approx 0.6(R_2 - R_\star)$. Actually, the most important parameter that determines the stellar wind structure is f_{tot} and the other parameters, R_1 , R_2 , σ_1 , σ_2 , $f_{1,\text{tot}}$, and $f_{2,\text{tot}}$, only give small corrections.

We dynamically solve ideal MHD equations with radiative cooling and thermal conduction. Conservation of mass, momentum (both radial and tangential components), and energy, and evolution of magnetic field are respectively expressed as

$$\frac{d\rho}{dt} + \frac{\rho}{r^2 f} \frac{\partial}{\partial r} (r^2 f v_r) = 0, \quad (3)$$

$$\rho \frac{dv_r}{dt} = -\frac{\partial p}{\partial r} - \frac{1}{8\pi r^2 f} \frac{\partial}{\partial r} (r^2 f B_\perp^2)$$

$$+ \frac{\rho v_{\perp}^2}{2r^2 f} \frac{\partial}{\partial r} (r^2 f) - \rho \frac{GM_{\star}}{r^2}, \quad (4)$$

$$\rho \frac{d}{dt} (r \sqrt{f} v_{\perp}) = \frac{B_r}{4\pi} \frac{\partial}{\partial r} (r \sqrt{f} B_{\perp}). \quad (5)$$

$$\rho \frac{d}{dt} \left(e + \frac{v^2}{2} + \frac{B^2}{8\pi\rho} - \frac{GM_{\star}}{r} \right) + \frac{1}{r^2 f} \frac{\partial}{\partial r} \left[r^2 f \left\{ \left(p + \frac{B^2}{8\pi} \right) v_r - \frac{B_r}{4\pi} (\mathbf{B} \cdot \mathbf{v}) \right\} \right] + \frac{1}{r^2 f} \frac{\partial}{\partial r} (r^2 f F_c) + q_R = 0, \quad (6)$$

$$\frac{\partial B_{\perp}}{\partial t} = \frac{1}{r \sqrt{f}} \frac{\partial}{\partial r} [r \sqrt{f} (v_{\perp} B_r - v_r B_{\perp})], \quad (7)$$

where ρ , \mathbf{v} , p , \mathbf{B} are density, velocity, pressure, and magnetic field strength, respectively, and subscript r and \perp denote radial and tangential components; $\frac{d}{dt}$ and $\frac{\partial}{\partial t}$ denote Lagrangian and Eulerian derivatives, respectively; $e = \frac{1}{\gamma-1} \frac{p}{\rho}$ is specific energy and we assume the equation of state for ideal gas with a ratio of specific heat, $\gamma = 5/3$; G is the gravitational constant; $F_c = \kappa_0 T^{5/2} \frac{dT}{dr}$ is thermal conductive flux by Coulomb collisions, where $\kappa_0 \approx 10^{-6}$ in c.g.s unit; q_R is radiative cooling. In this paper we assume the solar elemental abundance for the radiative cooling term. In sufficiently low density regions with $\rho \leq 5 \times 10^{-17}$ g cm $^{-3}$ we use optically thin radiative loss, $q_R = n_p n_e \Lambda$, where n_p and n_e are proton and electron number densities and Λ is the tabulated cooling function by Landini & Monsignori-Fossi (1990). In denser regions, which generally corresponds to low chromosphere, we adopt empirical radiative cooling, $q_R = 4.5 \times 10^9 \rho$ (erg cm $^{-3}$ s $^{-1}$) derived from observations of the solar chromosphere (Anderson & Athay 1989; Moriyasu et al. 2004) to take into account the optically thick effect. For simplicity's sake we switch off the cooling if temperature drops below 3000 K, which sometimes happens in the RGB stars. We might have to take into account effects of neutral atoms or dusts in such low temperature, though we do not do explicitly in this paper (see §4.3).

We adopt the second-order MHD-Godunov-MOCCT scheme (Sano & Inutsuka 2007 in preparation; see also SI06) to update the physical quantities. In this scheme each cell boundary is treated as a discontinuity, and for the time evolution we solve the nonlinear Riemann shock tube problem with magnetic pressure by using the Rankine-Hugoniot relations. Therefore, entropy generation, namely heating, is automatically calculated from the shock jump condition. A great advantage of our code is that no artificial viscosity is required even for strong MHD shocks; numerical diffusion is suppressed to the minimum level for adopted numerical resolution.

2.3. Surface Conditions

We describe the conditions of the stellar photospheres, which are the inner boundaries of the simulations.

2.3.1. Density

The density, ρ_0 , at photosphere (defined as optical depth ≈ 1) is subject to stellar parameters through various opacity effects in the atmosphere. The gas pressure, p_0 , at photosphere has a positive dependence on gravity, $p_0 \propto g^{0.6}$, for a given T_{eff} (§9 of Gray 1992).

p_0 has a negative dependence on T_{eff} , and in the cool star condition ($4000 \text{ K} \lesssim T_{\text{eff}} \lesssim 6000 \text{ K}$) the relation is roughly $p_0 \propto T_{\text{eff}}^{-2}$ (Figure 9.21 of Gray 1992). Then, $\rho_0 (\propto p_0/T_{\text{eff}})$ can be scaled as

$$\rho_0 \propto g^{0.6} T_{\text{eff}}^{-3}. \quad (8)$$

We firstly set $\rho_0 = 10^{-7}$ g cm $^{-3}$ on the sun and ρ_0 's in the other cases are determined by this scaling relation; ρ_0 's in Table 1 are thus given².

2.3.2. Wave Amplitude

The fluctuation amplitude, δv_0 , at the photospheres can be estimated from convective flux. The generation of sound waves on late-type stars have been extensively studied (Lighthill 1952; Stein 1967; de Loore 1970; Renzini et al. 1977; Bohn 1984; Shibahashi 2005). Recently, numerical experiments of surface convection are also carried out (Stein et al. 2004). These works show a similar qualitative trend that the excited acoustic flux, $F_{a,0}$ (erg cm $^{-2}$ s $^{-1}$), has a negative dependence on surface gravity and a positive dependence on stellar effective temperature. In this paper we adopt the relation derived by Renzini et al. (1977),

$$F_{a,0} (\approx \rho_0 \langle \delta v_0^2 \rangle c_s) \propto g^{-0.7} T_{\text{eff}}^{12}, \quad (9)$$

where δv_0 is wave amplitude, c_s is sound speed, and $\langle \rangle$ denotes time-average.

Strictly speaking, δv_0 should be longitudinal (parallel to the field line; *i.e.* radial direction) component. In this paper we assume both transverse and longitudinal components have the same amplitude at the photosphere. This assumption is roughly satisfied at least on the sun because observation of solar granulations shows that both transverse and longitudinal amplitudes are similar, $\approx 1 - 2$ km s $^{-1}$ (Holweger et al. 1978). We set $\langle \delta v_0 \rangle = 1.0$ km s $^{-1}$ in the present sun (Model I), where $\langle \delta v_0 \rangle \equiv \sqrt{\langle \delta v_{\parallel,0}^2 \rangle}$. For the other stars, we can use the following scaling,

$$\langle \delta v_0 \rangle \propto g^{-0.65} T_{\text{eff}}^{7.25}, \quad (10)$$

which is derived from Equations (8) and (9) (note $c_s \propto T_{\text{eff}}^{1/2}$). $\langle \delta v_0 \rangle$'s in Table 1 are determined by this relation³.

2.3.3. Wave Spectrum

The typical period, τ , of generated waves is also related to stellar parameters. τ can be scaled by eddy (granulation cell) turn-over timescale, $\sim l/c_s$, where l is a typical granulation size, if stochastic processes of the convection dominate in the wave generation. l 's are different in different stars, and are probably proportional to the pressure scale heights, $H_p \approx c_s^2/g$. Then, we have

$$\tau \sim l/c_s \propto H_p/c_s \sim c_s/g \propto g^{-1} T_{\text{eff}}^{0.5}, \quad (11)$$

² ρ_0 's in Table 1 are slightly different ($< 10\%$) from the values derived from Equation (8) This is because ρ_0 's are set by the model atmosphere that is used to derive the approximated scaling of Equation (8).

³ $\langle \delta v_0 \rangle$'s in Table 1 are also slightly different from those based on Equation (10). This is again because we are using the model atmosphere when setting δv_0 .

which is consistent with recent numerical simulations (e.g. Stein et al. 2004).

We use Equation (11) to give the realistic spectra of fluctuations at the photosphere. In this paper, we adopt a broadband power spectrum of $P(\nu) \propto \nu^{-1}$ with respect to frequency, $\nu = 1/\tau$, where the normalization is given by $\langle \delta v_0^2 \rangle = \int_{\nu_{\min}}^{\nu_{\max}} d\nu P(\nu)$. For the present sun, we set $\tau_{\min} (= 1/\nu_{\max}) = 1$ min and $\tau_{\max} (= 1/\nu_{\min}) = 32$ min, giving the (logarithmic) mean value ≈ 5 min, which dominates the solar oscillations. τ_{\min} 's and τ_{\max} 's of the other stars can be determined by the scaling relation of Equation (11) as shown in Table 1. It should be noted that a shape of $P(\nu)$ affects wind structure little as long as the same τ_{\min} and τ_{\max} are adopted (SI06).

2.3.4. Wave Mode

In this paper we only consider the open field regions in which the (unperturbed) magnetic fields are oriented to the vertical direction at the surfaces. In such a situation, if we restrict waves traveling in the vertical direction, the transverse components of surface fluctuations produce Alfvén waves, while the longitudinal component excites compressive waves, e.g. acoustic waves, or more generally, magnetosonic waves. The uncompressive character enables the Alfvén waves to propagate long distance. On the other hand, the longitudinal waves are quite dissipative because both nonlinear shock formation (Suzuki 2004) and collisionless dissipation (Suzuki et al. 2006) are effective. Thus, the compressive waves cannot travel a sufficiently long distance to contribute to the acceleration of the winds (Suzuki 2002). Actually, we tested a role of longitudinal fluctuations in several models and found that its effect is limited in the regions near the surfaces ($\ll 2 R_*$). Therefore, we only show the results of transverse fluctuations at the photospheres in this paper.

3. RESULTS

We initially set up the static and cool atmospheres with the photospheric temperatures; *neither stellar winds nor hot coronae are set up in advance*. We start the simulations by injecting the transverse fluctuations from the photospheres, which excite Alfvén waves (see the *electronic edition* for the mpeg file of Model VI which is the movie version of Figure 5). The atmospheres are accelerated as transonic winds in all the six Models by the dissipation of the Alfvén waves (§3.4.2). This shows that the transonic outflow is a stable and natural consequence of the Alfvén wave-driven winds of both MS and RGB stars. The stellar winds are settled down to the quasi-steady states after \gtrsim twice of the sound crossing times of the entire simulation boxes (the sound speeds are slower than the Alfvén speeds in our simulations), although the RGB cases (Models III-VI) show large fluctuations in the winds by thermal instability (§3.2).

First we would like to briefly mention the main results of our simulations. Figure 3 presents the structure of temperature, T (K) (top), outflow velocity, v_r (km s $^{-1}$) (middle), and density, ρ (g cm $^{-3}$) (bottom) on radial distances from the stellar centers in unit of R_\odot . The quantities are averaged over sufficiently longer durations than τ_{\max} of each Model. Figure 4 shows the typical wind parameters, temperature, T (K) in the atmosphere (top),

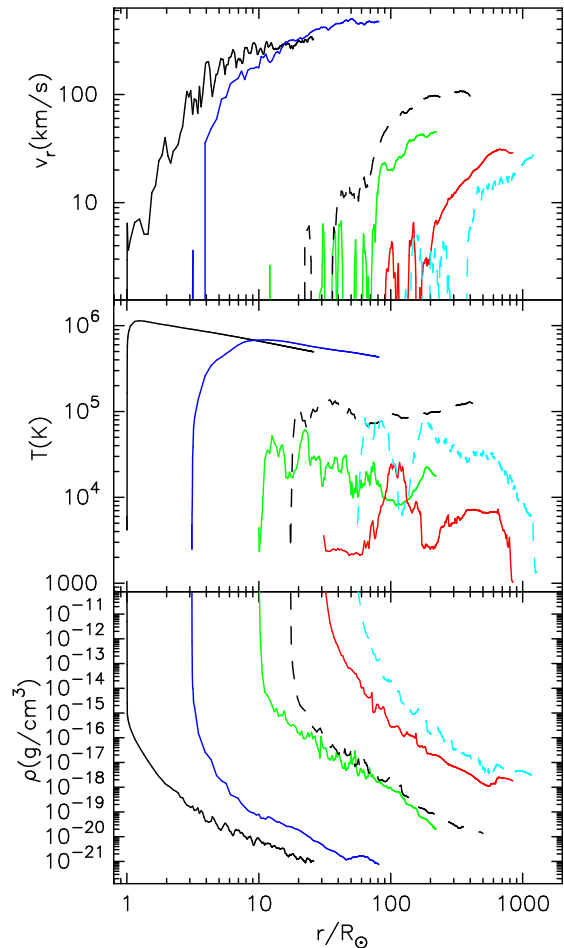


FIG. 3.— Time-averaged stellar wind structure of the six Models. From the top to the bottom, temperature, T (K), radial outflow velocity, v_r (km s $^{-1}$), and density, ρ (g cm $^{-3}$), are plotted. The solid lines are the results of the $1 M_\odot$ stars; the black, blue, green, and red lines are the results of Models I, II, III, and IV, respectively. The dashed lines are the results of the $3 M_\odot$ stars; the black and light-blue lines are the results of Models V and VI.

wind speed, V_{20R_*} (km s $^{-1}$), at $20 R_*$ (middle), and mass loss rate, $\dot{M} = 4\pi(\rho r^2 v)_{20R_*}$ (M_\odot yr $^{-1}$), evaluated at $20 R_*$ (bottom), as functions of $v_{\text{esc},0}$; evolved stars are in the left side. Note that the super-radial expansions of the flux tubes finish in $r < 3R_*$ so the flux tubes are radially oriented at $r = 20R_*$. In the top panel, we are averaging $T(r)$ in $1.5 - 15 R_*$. The solid error bars correspond to the temperature ranges of the time-averaged structure in this region. The dashed error bars in all the panels correspond to the maximum and minimum values from the snapshot results (§3.2).

One of the most important results is the disappearance of *steady* hot coronae in the RGB stars (Models III - VI). It is clearly seen in the top panel of Figure 4 that the average temperature drops suddenly from $T \simeq 7 \times 10^5$ K in the sub-giant star (Model II) to $T \leq 10^5$ K in the RGB stars. The large dashed error bars in the same panel indicate that the temperatures of the RGB atmospheres show large variations. One may also see in the middle and bottom panels that the velocities and mass loss rates of the RGB stars largely fluctuate. Particularly, \dot{M} 's of

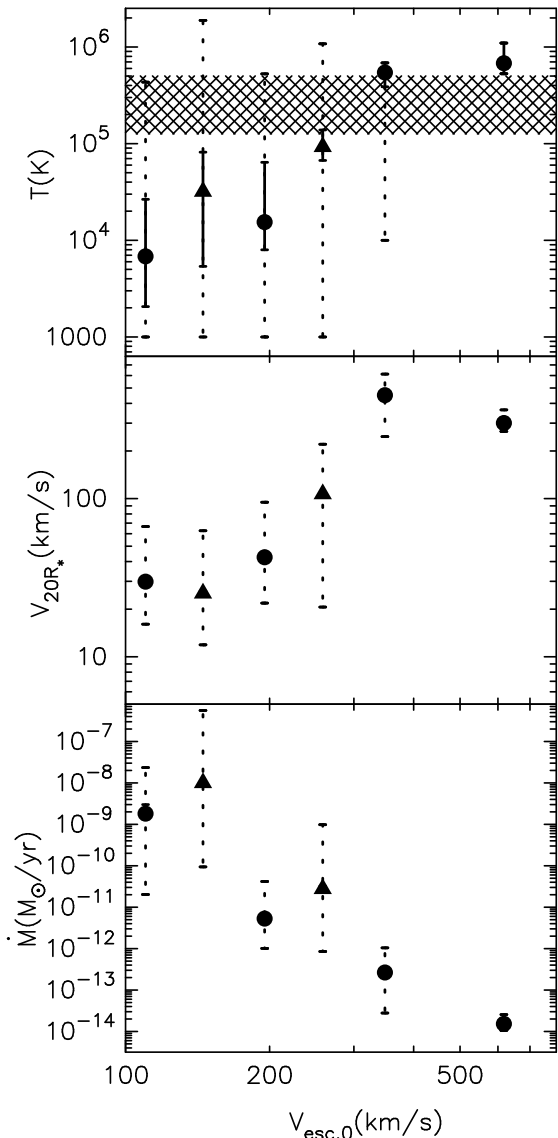


FIG. 4.— Typical wind parameters of the six Models as functions of surface escape velocity, $v_{\text{esc},0}$ (km s^{-1}). The circles and triangles represent the time-averaged values of the $1 M_{\odot}$ (Models I - IV) and $3 M_{\odot}$ (Models V & VI) stars, respectively. From the top to the bottom temperature, T (K), outflow velocity, evaluated at $r = 20 R_{\star}$ are plotted. T (K) is averaged over the range of $1.5 R_{\star} \leq r \leq 15 R_{\star}$. The solid error bars in the top panel correspond to the maximum and minimum values of the time-averaged structure in this range. The dashed error bars are the results of the maximum and minimum values derived from the snap-shot results (§3.2). The hatched region in the top panel indicates the thermally unstable region.

the RGB stars vary 2-4 orders of magnitude. Therefore, the red giant winds are highly structured, in contrast to the steady coronal winds from the MS and sub-giant stars.

The middle panel of Figure 3 shows that nearly-static regions are formed above the photospheres in the RGB stars, and the acceleration of the winds essentially starts from several stellar radii. Accordingly, their wind speeds in the outer regions are considerably slower than the escape velocities at the surfaces (the middle panel of Figure 4), which is consistent with the observed trend (*e.g.*

Dupree). The mass loss rate rapidly increases from MS to RGB. The average \dot{M} 's of the stars with $\log g = 1.4$ are $10^{-9} - 10^{-8} M_{\odot} \text{yr}^{-1}$, which are comparable to the observed level (Judge & Stencel 1991).

3.1. Disappearance of Steady Coronae

We explain the mechanism of the disappearance of the steady corona in more detail. The main reason is that the sound speed ($\approx 150 \text{ km s}^{-1}$) of $\approx 10^6 \text{ K}$ plasma exceeds the escape speed, $v_{\text{esc}}(r) = \sqrt{2GM_{\star}/r}$, at $r \gtrsim$ a few R_{\star} ; the hot corona cannot be confined by the gravity any more in the atmospheres of the RGB stars. Therefore, the material flows out before heated up to coronal temperature. However, the temperature gap at $v_{\text{esc},0} \simeq 300 \text{ km s}^{-1}$ (the top panel of Figure 4) cannot be explained only by this reason.

Thermal instability plays an important role in the drop of the temperature. The radiative cooling function of the optically thin gas with the solar abundance (Landini & Monsignori-Fossi 1990) shows a decreasing trend on temperature in $T > 10^5 \text{ K}$, indicating that gas is less cooled as it is heated up. Then, thermal instability sets in and gas in this temperature range cannot stably exist (Koyama & Inutsuka 2002). In solar and stellar coronal situations, however, thermal conduction plays a role in stabilization; drastic heating to $T \sim 10^7 \text{ K}$ is suppressed by the downward conduction from the upper corona to the lower chromosphere (Hammer 1982). Then, gas with $T \gtrsim 10^6 \text{ K}$ becomes thermally stable, while gas with $10^5 \text{ K} < T \lesssim 10^6 \text{ K}$, which is shown by the hatched region in Figure 4, remains unstable.

Let us think about comparison of c_s and v_{esc} at a few R_{\star} of the $1 M_{\odot}$ stars. In Models I and II, v_{esc} exceeds c_s ($\approx 150 \text{ km s}^{-1}$) of 10^6 K plasma. Under such a condition the coronal temperatures are determined by energy balance among heating, radiative cooling, and downward thermal conduction in the transition region which divides the chromosphere and the corona (Hammer 1982). However, in Model III ($\log g = 2.4$) $v_{\text{esc}}(3R_{\star}) \sim 110 \text{ km s}^{-1}$, and in Model IV ($\log g = 1.4$) $v_{\text{esc}}(3R_{\star}) \sim 60 \text{ km s}^{-1}$, which correspond to sound speeds of plasmas with $T \simeq 6 \times 10^5 \text{ K}$ and $\simeq 2 \times 10^5 \text{ K}$, respectively. Therefore, the gas streams out before heated up to the stable temperature ($\gtrsim 10^6 \text{ K}$) because of the insufficient confinement by the gravity. Those temperatures are thermally unstable, and then, the actual temperatures become lower than the gravity limited values. This is the reason why the average temperatures of Models III - VI are not $10^5 - 10^6 \text{ K}$ but $< 10^5 \text{ K}$. In conclusion, the thermal instability, in addition to the gravity effect, yields the sharp decline of the temperature from $T \gtrsim 10^6 \text{ K}$ to $T \lesssim 10^5 \text{ K}$ with the stellar evolution.

The results (Figures 3 & 4) show that the temperatures in the winds of the $3 M_{\odot}$ RGB stars are systematically higher than those of the $1 M_{\odot}$ counterparts. This is because the energy inputs from the surfaces are larger in more massive stars. When fixing surface gravity, a star with a larger mass has higher effective temperature, which gives a larger photospheric amplitude (Equation 10). Then, more energy is injected from the surface so that the larger heating is achieved.

3.2. Structured Red Giant Winds

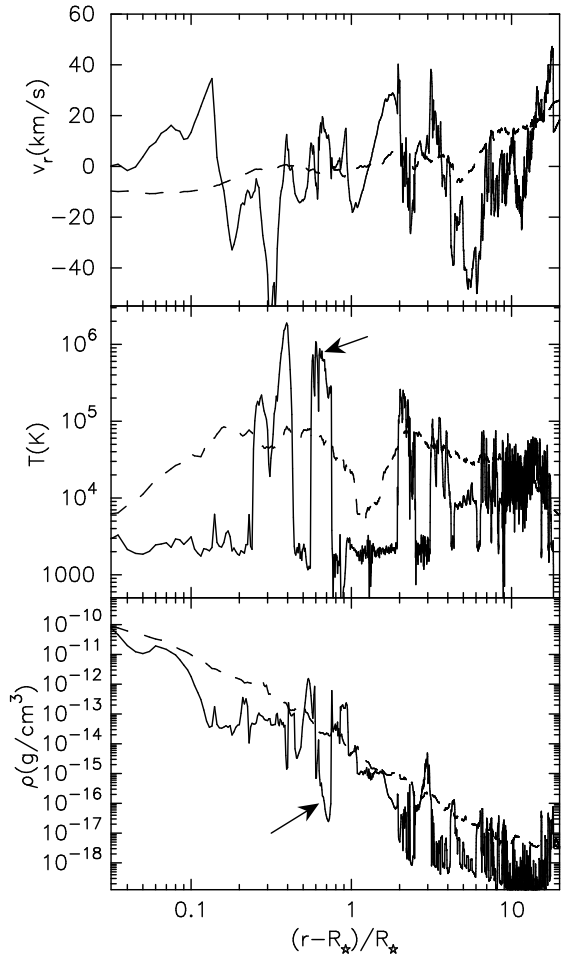


FIG. 5.— Snap-shot wind structure (solid) of Model VI at $t = 6909$ (hr), compared with the time-averaged structure (dashed). From the top to the bottom, v_r (km s $^{-1}$), T (K), and ρ (g cm $^{-3}$) are plotted on $(r - R_*)/R_*$. The arrows in the middle and bottom panels show the magnetized hot bubble which we inspect in §3.2.1 and Figure 6. The mpeg movie which shows this simulation from $t = 0$ to 9800 hr is available in the *electronic edition*. The movie file presents $\langle v_{\perp} \rangle$ (km s $^{-1}$) in addition to v_r (km s $^{-1}$), T (K), and ρ (g cm $^{-3}$).

After the disappearance of the steady corona, the atmospheres and winds of the RGB stars show time-dependent behaviors because of the thermal instability. In this section, we examine the snap-shot structure of the red giant winds. We firstly show the results of Model VI ($3 M_{\odot}$), which is redward of the DL but more active than the $1 M_{\odot}$ counterpart (Model IV). After that, we discuss the other RGB cases.

Figure 5 shows the snap-shot wind structure of Model VI at $t = 6909$ (hr) (solid) in comparison with the time-averaged structure (dashed) that is the same as in Figure 3. The mpeg movie of the simulation is also available in the *electronic edition*. Figure 5 illustrates that the simple picture of layered atmosphere, photosphere – chromosphere – transition region – corona – wind from below, does not hold in the RGB star. A characteristic feature is that a number of hot bubbles with low densities are distributed in cool background material. For example, in an inner region ($r - R_* < R_*$) the two bubbles with the peak temperatures $> 10^6$ K are seen; in $R_* < r - R_* \lesssim 10 R_*$ a

couple of warm bubbles with $T \gtrsim 10^5$ K are formed. The hot and warm bubbles and the cool background materials are connected by the transition regions, at which the temperature drastically changes because of the thermal instability.

The densities of the hot bubbles are lower than the ambient media to satisfy the pressure balance. As seen in the bottom panel of Figure 5 the density fluctuates typically by 2-3 orders of magnitude in the wind, which is related to the fact that the gas mainly consists of hot ($> 10^6$ K) and cool ($< 10^4$ K) components. Strictly speaking, however, magnetic pressure also needs to be taken into account for the force balance (§3.2.1). The outflow speed fluctuates as well to fulfill the mass conservation relation. The red giant wind is not a steady outward stream but an outflow consisting of many small-scale structures. Our simulation shows that both hot plasma and cool chromospheric wind coexist in the RGB star, which is consistent with observations of hybrid stars (Hartmann, Dupree, & Raymond 1980; Harper et al. 1995; Ayres et al. 1998).

3.2.1. Magnetized Hot Bubble

How are these hot bubbles formed? How are the high temperatures maintained? We study the formation and evolution of bubbles by inspecting one typical hot bubble that is indicated by the arrows in Figure 5. This bubble is initially created at $r = 1.04 R_*$ at $t = 6755$ hr. It comoves outwardly with the background flow and eventually cooled down to $\approx 10^4$ K at $t \approx 7070$ hr at $r = 1.6 R_*$ (see the mpeg movie of Figure 5 available in the *electronic edition*).

Figure 6 presents the zoomed-in structure just after the formation of the bubble (the lower panels) with schematic cartoon (top). The location of the shock front, which plays a role in the heating of the bubble, is indicated by the dotted line at $r = 1.047 R_*$ in the panels. The top and middle panels show $p_B (= B_{\perp}^2/8\pi$; magnetic pressure), p , v_r , T and ρ . In the bottom panel, we present heating rate per mass. The solid line indicates the net heating rate that is calculated from local change of specific heat, $\partial e/\partial t$, and the dashed line shows the heating by the only MHD process which excludes radiative cooling and thermal conduction from $\partial e/\partial t$.

As clearly seen in the bottom panel the heating rate is not smoothly distributed but largely fluctuates because the heating mainly occurs at the steepened fronts of waves (see §3.4.2). Radiative cooling is also important; in some portions the net heating becomes negative (the solid lines disappears) in spite of the positive MHD heating (dashed line), because the radiative cooling exceeds the MHD heating. This large variation of the heating rate by waves and cooling triggers the multi-temperature stellar wind.

p_B increases at the shock front from the upstream (right) side to the downstream (left) side, which indicates that this is a fast MHD shock. One may find the density peak just behind the shock front. This is because an effective ratio of specific heats is small $\gamma_{\text{eff}} \lesssim 1.1$ owing to the thermal conduction; the density jump at the shock becomes large in small γ_{eff} circumstances so that the material should be concentrated in the narrow region behind the shock to satisfy the mass conservation (Kim & Ryu 2005). As a result, the radiative cooling

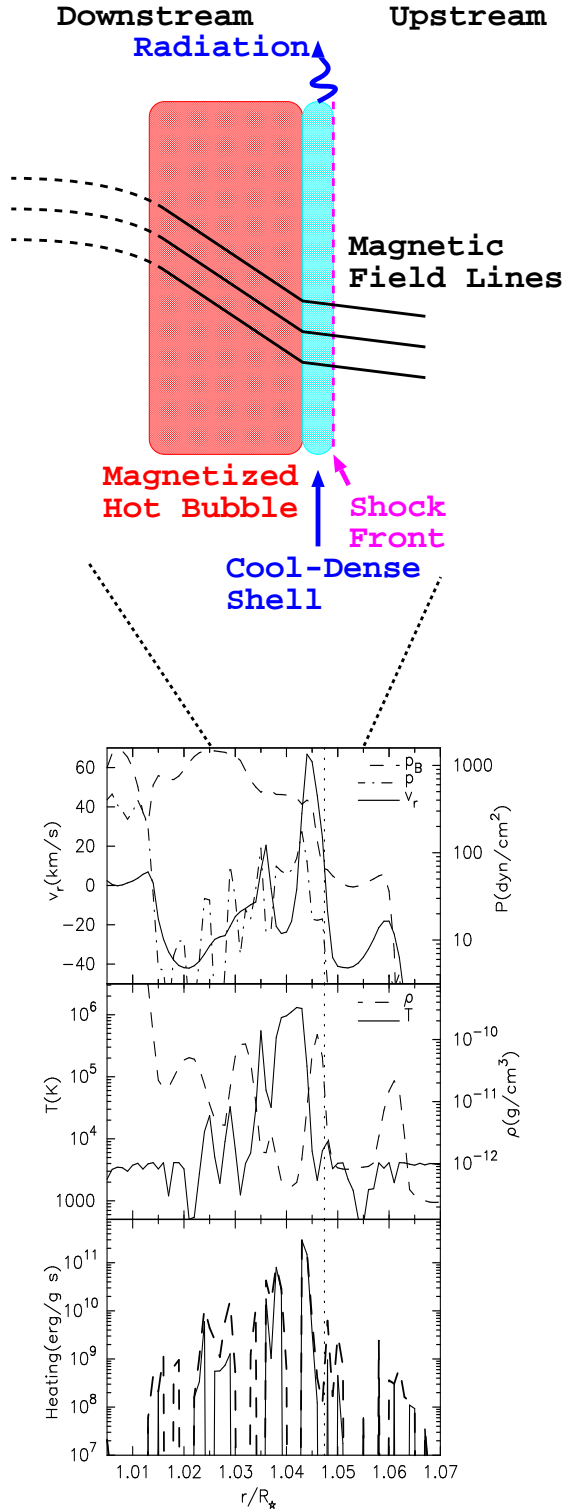


FIG. 6.— Zoomed-in structure of the magnetized hot bubble at $t = 6755$ (hr) (lower panels), which is the initial phase of the bubble indicated by the arrows in Figure 5, and schematic picture of a magnetized hot bubble (upper cartoon). The dotted lines in the lower panels show the location of the shock front. What are plotted in the lower three panels are as follows: *top*: The dashed, dot-dashed, and solid lines are magnetic pressure, $p_B = B_{\perp}^2/8\pi$, gas pressure, p , and radial velocity, v_r . The values of p and p_B are on the right axis (dyn cm $^{-2}$) and the value of v_r is on the left axis (km s $^{-1}$). *middle*: The solid and dashed lines are temperature (K; left axis) and density (g cm $^{-3}$; right axis). *bottom*: The vertical axis shows heating rate (erg g $^{-1}$ s $^{-1}$). The solid line is the net heating derived from the change of specific heat and the dashed line is the pure MHD heating which excludes the effect of radiative cooling and thermal conduction from the net heating.

dominates the MHD heating owing to the high density, and this region is cooled down to form a cool dense shell (the bottom panel of Figure 6).

Behind this cool dense shell, the hot region, which was heated up by the fast MHD shock, remains. The fast MHD shock plays an important role in maintaining this hot bubble. Because the magnetic field is generated by the shock, the magnetic pressure in the bubble is larger than in the ambient gas. Therefore, the hot bubble is not supported by the gas pressure but by the magnetic pressure. Even though the gas pressure decreases by an occasional cooling, the bubble can avoid being compressed. The density is kept low to reduce the radiative loss as well as to increase the heating rate per mass. The hot bubble survives much longer time than ambient (average) cooling time until the magnetic topology changes; the high temperature is maintained around 315hr, while a typical cooling time, τ_{cool} , of gas with $T = 10^6$ K ($\Lambda \approx 10^{-22}$ erg cm 3 s $^{-1}$; see §2.2) is

$$\tau_{\text{cool}} = \frac{\rho e}{q_R} \approx 1 \text{ min} \left(\frac{\rho}{10^{-13} \text{ g cm}^{-3}} \right)^{-1} \quad (12)$$

To summarize, hot bubbles are initially created by the variations of heating rate, and their high temperature is maintained thanks to the support by magnetic pressure.

An intriguing concept of magnetized hot bubbles is that hot plasma can be heated up even in open field regions. It has been generally considered that closed loops are necessary to confine hot plasma in the atmosphere of a RGB star since the gravity is not sufficiently strong. However, our simulations show that the hot bubble can exist rather long time (~ 10 days) by magnetic topology, *i.e.* a fast MHD shock, in open field regions. It is supposed that such hot bubbles are ubiquitously created and they are possible sources of continuous soft X-ray emissions in hybrid stars as discussed later (§3.2.3).

3.2.2. Time-Variation of Wind Parameters

Because the red giant wind consists of many small-scale structures, the mass loss rate and the outflow speed in the outer region also show time-dependent behaviors. Figure 7 presents \dot{M} (M_{\odot} yr $^{-1}$) (upper) and $v_{20 R_{\star}}$ (km s $^{-1}$) (lower). The upper panel shows \dot{M} varies more than three orders of magnitude from 1×10^{-10} to 5×10^{-7} M_{\odot} yr $^{-1}$. The lower panel also shows that $v_{20 R_{\star}}$ largely varies from 10 km s $^{-1}$ to 60 km s $^{-1}$.

The jumps are seen in \dot{M} and $v_{20 R_{\star}}$ at $t = 7200, 8750,$ and 9020 hr. These jumps indicate that dense blobs pass at $r = 20 R_{\star}$ at those times. We examine one of the blobs which passes at $t = 7200$ hr (This blob is seen in Figure 5 as well). This is a shock wave originally formed in an inner region. The shock amplitude has been initially small, but it grows as the shock moves outward by sweeping-up a number of smaller dense blobs as well as by amplification in the stratified atmosphere with the decreasing density. Finally the compression ratio of the shock increases to more than 10. (This value exceeds the adiabatic limit = 4 since our simulations, which take into account cooling and thermal conduction, are not adiabatic.) Before this shock arrives, \dot{M} is almost constant and $v_{20 R_{\star}}$ shows smoother feature. After the shock reaches $20 R_{\star}$, both \dot{M} and $v_{20 R_{\star}}$ show fluctuating be-

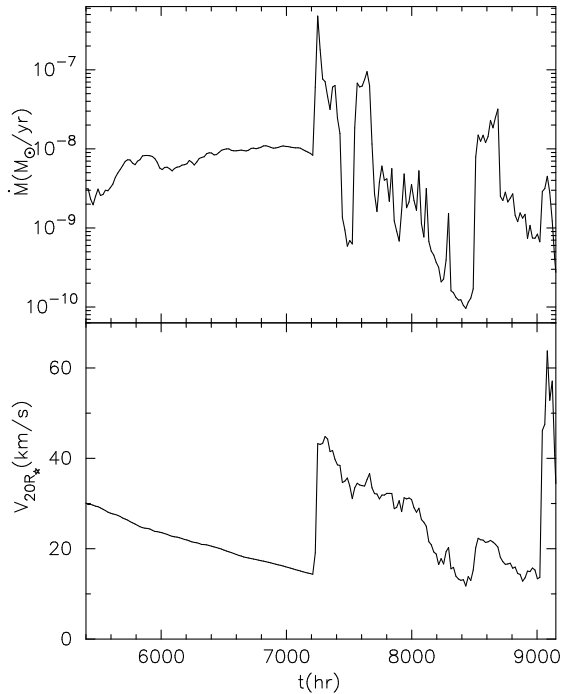


FIG. 7.— Mass loss rate (upper) and radial velocity (lower) of the stellar wind of Model VI as functions of time. Both quantities are evaluated at $r = 20 R_*$.

haviors. This is because the downstream region contains larger perturbation than the upstream region.

3.2.3. Radiative Flux

Hot bubbles in RGB atmospheres become sources of soft X-ray and extreme UV (EUV) radiation that is observed in hybrid stars. We present the radiative fluxes, normalized by the bolometric luminosity, from the entire star of Models VI as functions of time in Figure 8. The blue, green and red lines are the radiative fluxes from the gas with $T \leq 2 \times 10^4$ K (optical; chromosphere), 2×10^4 K $< T < 5 \times 10^5$ K (UV; transition region) and 5×10^5 K $\leq T$ (EUV/soft X-ray; corona). We call them cool, warm, and hot components, respectively. We also plot the radiative flux of the gas with $T \geq 10^6$ K, which is a part of the hot component and corresponds to soft X-ray emission.

When deriving the radiative fluxes from the entire star, we assume spherical symmetry:

$$L(T_1 < T < T_2) = 4\pi \int dr r^2 q_R(T_1 < T < T_2), \quad (13)$$

where T_1 and T_2 are the minimum and maximum temperatures of each component. While our simulations only treat the open magnetic field regions, in reality a certain fraction of the surface is covered by closed structures. Equation (13) assumes that the radiative fluxes from both open and closed regions have the same r dependence. Although this treatment is not strictly correct, we can give rough estimates.

According to the upper panel of Figure 8, the hot component shows strong intermittent activities, while the cool component, which dominates the total radiative flux, stays roughly constant within $10^{-3} \lesssim L_{\text{cool}}/L_* <$

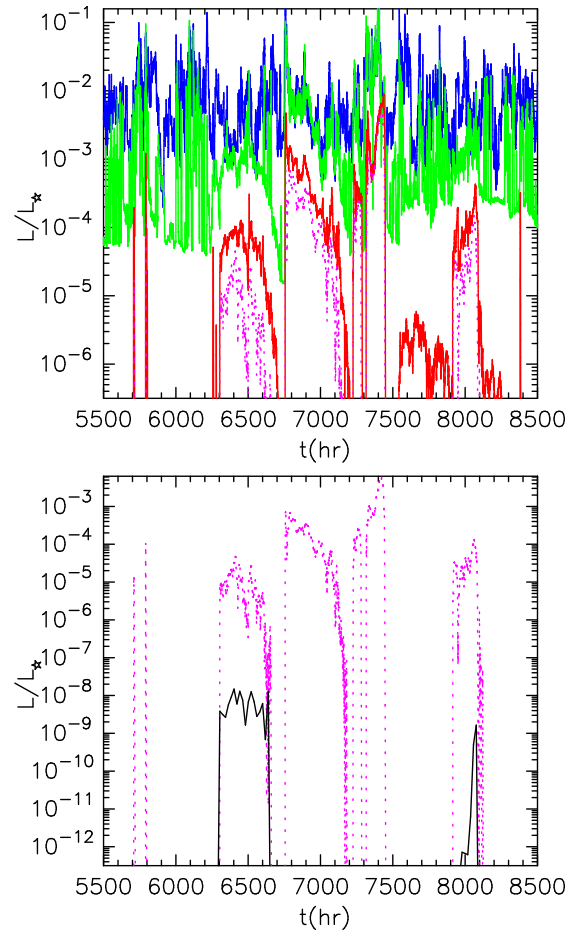


FIG. 8.— *Upper*: Normalized radiative fluxes, L/L_* , of cool ($T \leq 2 \times 10^4$ K; blue), warm ($2 \times 10^4 < T < 5 \times 10^5$ K; green), and hot ($T \geq 5 \times 10^5$ K; red) components of Model VI as functions of time elapsed from the beginning of the simulation. The radiative flux of $T \geq 10^6$ K gas, which is a part of the hot component, is also plotted (dashed line). *Lower*: Radiative flux of the soft X-ray ($T \geq 10^6$ K) that takes into account the absorption by the cool wind materials (black solid), in comparison with the original flux without the absorption (pink dashed).

10^{-1} . The behavior of the warm component is between the cool and hot ones; when the hot component is switched-off or stays in low activity phases (e.g. 7500–8000 hr) $L_{\text{warm}}/L_* \approx 10^{-4}$, but once the hot component becomes active, L_{warm}/L_* increases to $\gtrsim 10^{-2}$ by the contributions from the transition regions of hot bubbles.

It is also shown that the hot bubbles with $T \geq 10^6$ K exist during the only half of the presented duration. However, we should note that this is based on the spherical symmetry approximation. In reality, hot bubbles are created in different open flux tubes at different times, and they are ubiquitously distributed in the atmosphere to be continuous soft X-ray sources.

When discussing observed X-ray flux, we need to take into account the absorption by Hydrogen in the outer cool chromospheric wind (Ayres 2005). Then, the observed flux of the hot component would be smaller than that shown in the upper panel of Figure 8. In particular, soft X-ray radiation is supposed to severely suffer the ab-

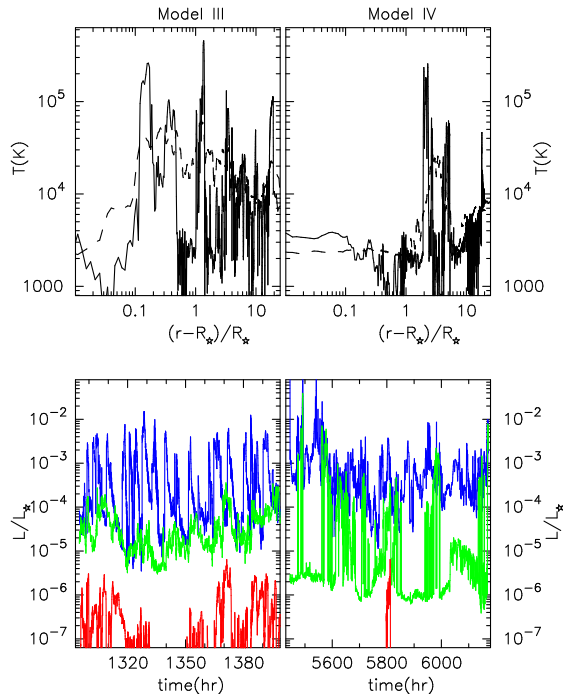


FIG. 9.— Temperature structure (upper panels) and time-variations of radiative fluxes (lower panels) of Models III (left panels) and IV (right panels). The snap-shot results of temperature (solid lines) are at $t = 1295$ and 6050 hr in Models III and IV, respectively. The time-averaged results that are the same as in Figure 3 are also shown by the dashed lines. The three components of the radiation is the same as in Figure 8.

sorption since most of the hot bubbles with $T > 10^6$ K are distributed in the inner region ($r \lesssim 2 R_*$).

In the lower panel of Figure 8 we compare the observed soft X-ray flux ($T \geq 10^6$ K) that takes into account the absorption (solid) with the original flux (dashed). Ten-fold obscuration of the soft X-ray emissions sets in at column density, $N_H = 5 \times 10^{20} - 5 \times 10^{21} \text{ cm}^{-3}$ (Ayres 2005). We adopt the most optimistic case of $N_H = 5 \times 10^{21} \text{ cm}^{-3}$:

$$L = \int dr r^2 q_R 10^{-N_H/5 \times 10^{21} \text{ cm}^{-3}}. \quad (14)$$

When deriving N_H from the simulation result, we only consider the gas with $T < 8000$ K to pick up neutral Hydrogen and assume the solar abundance. The lower panel of Figure 8 illustrates that most of the soft X-ray emissions are absorbed. Around $t \simeq 6500$ and 8000 hr, the soft X-ray could be observed, and the L_X/L_* is reduced to $\lesssim 10^{-8}$ from $10^{-5} - 10^{-4}$. Interestingly, this value, $L_X/L_* \lesssim 10^{-8}$, is typical for hybrid stars (e.g. Ayres 2005), although our calculation, which is based on 1D and do not consider detailed radiative processes, is too simplified for further quantitative arguments.

3.2.4. Other RGB Cases

We have examined the time-dependent behaviors of the $3 M_\odot$ red giant wind (Model VI). In this subsection we study the $1 M_\odot$ stars on both blueward (Model III) and redward (Model IV) sides of the DL. Figure 9 shows the snap-shot temperature structure and the time-variation of the radiative fluxes of Models III and IV. The upper panels (temperature) show that the atmospheres and

winds of the $1 M_\odot$ RGB stars also consist of many hot and warm bubbles embedded in the cool chromospheric materials. It is confirmed that RGB winds are generally structured with many blobs and bubbles.

The temperature of bubbles are lower in the more evolved star (Model IV). This trend is also clearly seen in the plots of the radiative fluxes (the lower panels). The emission from the hot gas ($T > 5 \times 10^5$ K) exists only during the short term ($t = 5800$ hr) in Model VI, while the hot bubbles with $T > 5 \times 10^5$ K almost always exist in Model III. Namely, once a star with $1 M_\odot$ crosses the DL, EUV/soft X-ray emissions from hot plasma with $T > 5 \times 10^5$ K happen to disappear. However, the qualitative wind features, hot/warm bubbles in cool materials, are similar in Models III and IV. Both temperature and the number of hot bubbles decrease with the evolution from Models III to IV, because the heating rate per mass decreases on account of the increase of the density in the atmosphere (Figure 3).

The emission levels of the hot components of the $1 M_\odot$ stars are smaller than that of the $3 M_\odot$ star. This is because δv_0 (Table 1) of the surface convection is smaller in a less massive star owing to the lower T_{eff} (Equation 10). Our result is consistent with the observed trend that UV/X-ray emission of RGB stars are positively correlated with stellar mass (Hünsch & Schröder 1996).

The average emission level of the hot component of Model III is $L_{\text{hot}}/L_* \approx 10^{-6}$, which is marginally smaller than the typical observed X-ray flux ($L_X/L_* = 10^{-7} - 10^{-4}$; e.g. Ayres 2005) from RGB stars blueward of the DL. Moreover, the emissions are mostly from the bubbles with $T \lesssim 10^6$ (K) in our simulation, corresponding to EUV rather than soft-X ray emissions, and the effect of the absorption will further reduce the observed flux. Then, it would be difficult to explain the observed X-ray from RGB stars before crossing the DL by only the hot bubbles in open field regions. Probably, hot plasma, which is efficiently confined in closed magnetic loops, also contribute to the X-ray emission. Incidentally, Rosner et al. (1995) speculated that the DL was reflection of the change of magnetic topology; as a star crosses the DL, the magnetic structure becomes open and the hot plasma is liberated to be X-ray deficient (see §4.1).

3.3. Slow Red Giant Winds

The wind velocity also drastically decreases along with the stellar evolution as shown in Figure 4. As briefly stated previously, this is mainly because the nearly static regions are formed above the photospheres in the RGB stars and the winds are essentially accelerated from the effective surfaces located several R_* . We see this in more detail here. In order to investigate the drastic change of the wind speed, we compare Models near the transition at $v_{\text{esc},0} = 200 - 300 \text{ km s}^{-1}$ (the top panel of Figure 4). Figure 10 shows the simulated density structure (solid) of Models II (left), V (middle), and III (right), in comparison with the density structure based on hydrostatic equilibrium (dotted) and that derived from assumed constant velocities (dashed).

Hydrostatic equilibrium gives

$$\rho = \rho_1 \exp \left(\frac{GM_*}{a_{\text{eff}}^2} \left[\frac{1}{r} - \frac{1}{r_1} \right] \right)$$

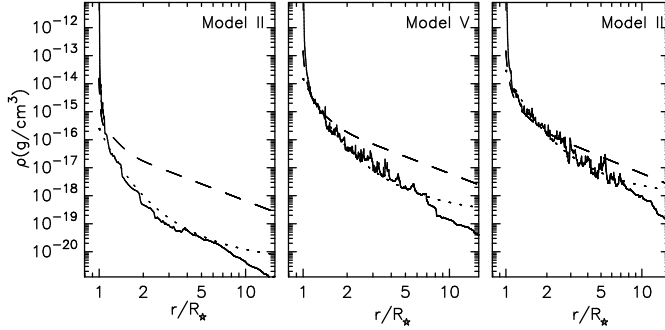


FIG. 10.— Density structure of Model II (left), V (middle), and III (right). The results are the same as in Figure 3 but compared with the densities derived from constant wind speeds (dashed lines) and from the hydrostatic equilibrium (dotted lines) (see text).

$$= \rho_1 \exp\left(-\frac{g_1}{a_{\text{eff}}^2} \frac{r_1}{r} z\right), \quad (15)$$

where r_1 is a certain reference position, $z \equiv r - r_1$, $g_1 = GM_*/r_1^2$, and ρ_1 is the density at $r = r_1$. We here assume the “isothermal” atmosphere with an effective sound speed, $a_{\text{eff}} = a^2 + B_{\perp}^2/8\pi\rho$, which takes into account magnetic pressure associated with Alfvén waves in addition to gas pressure, where a is isothermal sound speed. For Models II, V, and III, we adopt $a_{\text{eff}} = 74, 55$, and 43 km s^{-1} , respectively, which are estimated from the simulation results. We set r_1 at the coronal base (Model II) or the locations where the average temperatures start to increase (Models III & V). Note that $r_1 \simeq (1.01 - 1.02)R_*$ in these Models (see Figure 11 in §3.4.1). Figure 10 shows that the densities in the subsonic (inner) regions can be approximated by the hydrostatic structure, which is consistent with the result of general stellar wind theory (*e.g.* section 3 of Lamers & Cassinelli 1999). This indicates that the atmospheres are supported by both magnetic and gas pressure.

The dashed lines plot

$$\rho \propto (r^2 f)^{-1}, \quad (16)$$

which is derived from substituting constant v_r into the steady-state continuity equation of mass, $\rho v_r r^2 f = \text{const}$. The starting point is set in the low chromosphere in each Model. Because in Model II (the left panel) the density decreases faster due to the stronger gravity, the dashed line is far above the solid as well as dotted lines. This indicates the acceleration of the wind should start near the surface.

On the other hand, in Models III (the right panel) the decrease of the density is slower since the gravity is weaker. As a result, the solid line follows the dashed line in the inner region, which indicates that the wind is not accelerated, but stays almost a constant speed. The solid line is gradually diverging from the dashed line around $R_{\text{eff}} \approx \text{several } R_*$, which we call an “effective” surface, and at which the wind starts to be practically accelerated. In $r \lesssim R_{\text{eff}}$, the average wind speed is kept much slower than $10 \text{ km s}^{-1} (\ll c_s)$, and the atmosphere is almost static, as seen in Figure 3; the acceleration is not effective there because of too much material. The longitudinal motions seen in this region in the top panel of Figure 3 are not by outflow but due to compressive

waves (§3.4.2). The wind structure of the other RGB stars (Models IV and VI) is essentially similar to that of Model III.

The gravity is smaller at $r = R_{\text{eff}}$ than at the surface, hence the slow wind can escape outwardly. Therefore, we can expect that the terminal velocity is not an order of the surface escape speed but an order of the escape speed, $v_{\text{esc}}(R_{\text{eff}})$, at $r = R_{\text{eff}}$. This can explain why observed wind speeds are much smaller than the surface escape velocities in RGB stars (*e.g.* Dupree 1986). In Model III we can set $R_{\text{eff}} \simeq 8R_*$, hence, $v_{\text{esc}}(R_{\text{eff}}) \simeq 70 \text{ km s}^{-1}$. This value is an order of the terminal velocity which is supposed to be slightly faster than the obtained $v_{20R_*} = 40 - 50 \text{ km s}^{-1}$ when the effect of the acceleration in $r > 20R_*$ is taken into account.

The situation of Model V (the middle panel) is between Models II and III. The simulated density follows the trend of the non-acceleration at the beginning. However, the solid line departs from the dashed line earlier than in Model III. In this case the wind becomes gradually accelerated from a few R_* . Setting $R_{\text{eff}} \approx 3R_*$, we have $v_{\text{esc}} \approx 150 \text{ km s}^{-1}$ which is an order of the obtained v_{20R_*} . The difference between Models III and V arises from the difference of the radii; although these two Models have the same g , the decrease of the density is faster in Model V when measured in r/R_* , ($z = r - R_*$ is larger in Equation 15).

In concluding, we have the natural conclusion that the wind speed is determined by the escape speed at $r = R_{\text{eff}}$ where the wind practically starts to flow out. R_{eff} does not coincide with the stellar surface but moves outward as a star expands. Therefore, the wind speeds of the RGB stars are slower than the surface escape speeds.

3.4. Energetics

The main energy that drives the stellar winds is the turbulent energy of the surface convection in our simulations. The Alfvén waves that are excited by the footpoint motions of open flux tubes carry the energy outwardly and the dissipation of the waves leads to the heating and acceleration of the stellar winds. In this subsection, we quantitatively investigate the energetics of the stellar winds driven by Alfvén waves, and finally determine the mass loss rate in a *forward* manner.

3.4.1. Heating

We study the structure of lower atmosphere because it is important not only in determining the basal properties of the stellar winds but in controlling the reflection of the Alfvén waves. In Figure 11 we show the time-averaged density (top) and temperature (middle) which are the same as in Figure 3 but plotted on $(r - R_*)/R_*$ to enlarge the inner regions. Note that the physical distance (*e.g.* km) of the horizontal axis becomes larger for a star with larger R_* . In the bottom panel plasma β values defined as

$$\beta \equiv \frac{8\pi p}{B^2} \quad (17)$$

are plotted.

In the MS (Model I) and sub-giant (Model II) cases, the steady corona lies above the (geometrically) thin chromosphere and these two regions are divided by the sharp transition region. In the RGB cases (Models III-VI),

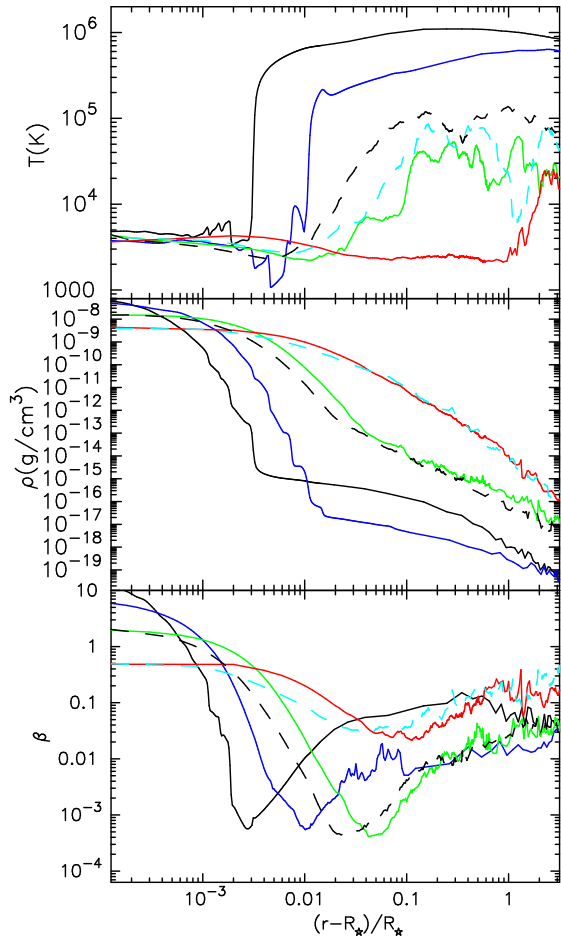


FIG. 11.— Structure of the inner regions of the six Models. From the top to the bottom, T (K), ρ (g cm^{-3}), and plasma β values are shown on $(r - R_*)/R_*$. The results in the top and middle panels are the same as in Figure 3. The solid lines are the results of the $1 M_\odot$ stars; the black, blue, green, and red lines are the results of Models I, II, III, and IV, respectively. The dashed lines are the results of the $3 M_\odot$ stars; the black and light-blue lines are the results of Models V and VI.

the temperature gradually increases outwardly from the chromosphere. This increase of the temperature is different from the formation of “warm corona” but the result of the time-average of intermittent creation of hot bubbles; the location at which the temperature increases is the starting point of the formation of hot bubbles. However, it is still worth studying the average trend from an energetics point of view.

The lower panel illustrates that the variations of β 's are qualitatively similar in the stars with $\log g = 2.4 - 4.4$; the β values decrease outwardly to $\sim 10^{-3}$ but turn to increase from certain locations. This is because when the magnetic pressure dominates the gas pressure by ~ 1000 times, the dissipation of a small fraction of magnetic energy gives an enormous effect on the gas. Indeed, the energy transfer from the magnetic fields to the plasmas is carried by the dissipation of the Alfvén waves in our simulations and the gas is heated up before β becomes further smaller. As the temperatures rise, the decreases of the densities become slower (Equation 15) and β 's increase due to the decreases of B 's. The densities at which the average temperatures start to increase are controlled

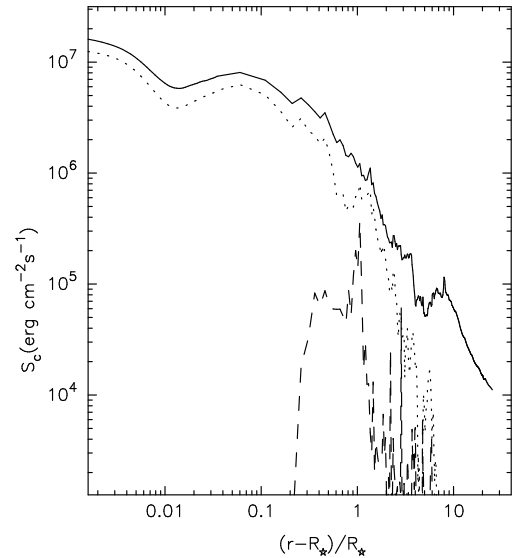


FIG. 12.— Adiabatic constants, S_c 's ($\text{erg cm}^{-2}\text{s}^{-1}$), of outgoing Alfvén (solid), incoming Alfvén (dotted), and outgoing slow (dashed) MHD waves in Model III.

in order that the plasma β values do not become too small. The geometrical depth of the inner chromosphere (the region between the photosphere and the location of temperature rise) is larger in a lower $\log g$ star since the decrease of density is slower.

In the stars with $\log g = 1.4$, the β values do not become as small as the other cases since the decreases of the densities in the low chromospheres are too slow to achieve such small β 's. Therefore, strong heating does not occur and the average temperatures are lower than the higher gravity stars.

In the $3M_\odot$ stars the temperatures start to increase from more inner positions than in the $1M_\odot$ counterparts. This is because a more massive star gives larger photospheric amplitude and input energy of Alfvén waves (Equation 10). Then, hot bubbles are heated up from a deeper (*i.e.* denser) region.

3.4.2. Dissipation and Reflection of Waves

In SI05 and SI06, we claimed that the nonlinear generation of MHD slow (\approx sound) waves is the main dissipation process in our 1D simulation of the solar wind; the energy of Alfvén waves is transferred to the slow waves, which dissipate by shocks after steepening of the wave fronts. We show that the same mechanism operates in RGB stars at least under the 1D approximation. We firstly inspect the dissipation processes by using the results of Model III, and after that, we compare the four cases of the $1 M_\odot$ stars (Models I-IV).

We are injecting the broadband spectra of the surface fluctuations and in the upper regions not only outgoing but incoming waves of different modes travel simultaneously. Hence, the actual simulations show turbulence-like feature (*e.g.* see v_\perp in the movie of Figure 5 available in *electric edition*). A technique of the mode decomposition (Cho & Lazarian 2003) is a useful tool to study such turbulent phenomena. Figure 12 plots the following adiabatic constants derived from wave action (Jacques

1977),

$$\mathcal{S}_c = \rho \langle \delta v_w^2 \rangle \frac{(v_r + v_{\text{ph}})(\mathbf{v}_r + \mathbf{v}_{\text{ph}})}{v_{\text{ph}}} \frac{r^2 f(r)}{r_c^2 f(r_c)}, \quad (18)$$

for outgoing Alfvén, incoming Alfvén, and outgoing slow MHD (sound) waves of Model III as functions of distance, where δv_w and \mathbf{v}_{ph} are amplitude and phase speed of each wave mode. In our simple 1D geometry, Alfvén waves are purely transverse and slow MHD waves are purely longitudinal; the energy flux of Alfvén waves is calculated from v_\perp and B_\perp , and the energy flux of slow MHD waves is from fluctuating components of v_r and ρ . A characteristic feature of incoming (outgoing) Alfvén waves is that v_\perp and B_\perp are in (in opposite) phase. The decomposition of each wave mode can be done by using these facts⁴. The subscript, c , denotes that \mathcal{S} is normalized at r_c where the flux tubes expand by $f_c = 40$, to exclude the effect of the adiabatic loss.

\mathcal{S}_c can be used as a measure of the dissipation. Although \mathcal{S}_c and energy flux are identical in static media, they are different in moving media. \mathcal{S}_c is conserved in expanding atmosphere if a wave does not dissipate, while it is not the case for the energy flux. For the incoming Alfvén wave, we plot the opposite sign of \mathcal{S}_c so that it becomes positive in the sub-Alfvénic region.

Figure 12 shows that the outgoing Alfvén waves dissipate quite effectively; $\mathcal{S}_c (= |\mathcal{S}_c|)$ becomes only $\sim 10^{-3}$ of the initial value at the outer boundary. First, a sizable amount is reflected back quite near the surface, which is clearly illustrated as the incoming Alfvén wave that is following the outgoing component with a slightly smaller level. This is because the wave shape is considerably deformed owing to the steep density gradient. In this region, the temperature is small, $T \simeq 3000$ K, which gives a short pressure scale height, H_P (Figure 11). Then, the wavelength of the Alfvén waves becomes comparable or longer than H_P , which results in the effective reflection of the waves (Moore et al. 1991). In this Model III, more than 60% of the initial energy flux of the Alfvén waves are reflected back before reaching the upper warm region with the *average* temperature, $\sim 10^5$ K (§3.4.3).

Second, slow MHD waves are generated in the corona (see Sakurai et al. 2002 for solar observation) as shown in Figure 12. The generation of the slow waves is triggered by the variation of the magnetic pressure, $B_\perp^2/8\pi$, with the Alfvén waves (Kudoh & Shibata 1999). This excites density perturbations, which are slow MHD waves in magnetically dominated plasma. Slow waves are generally longitudinal, and then, they eventually suffer nonlinear steepening to lead to shock dissipation (Suzuki 2002). The density fluctuations of slow waves also work as mirrors to Alfvén waves. The variation of the density directly leads to the variation of the Alfvén speeds ($\propto B/\sqrt{\rho}$), which enhances the reflection of the Alfvén waves by the deformation of the shape. These reflected waves further nonlinearly interact with the pre-existing outgoing waves, which plays a role in the dissipation.

⁴ This method is strictly valid only for linear and short wavelength waves of which amplitudes are sufficiently smaller than phase speed and wavelengths are sufficiently shorter than a variation scale of background phase speed (*i.e.* WKB approximation holds). For nonlinear and long wavelength waves, which we want to deal with, this treatment is only *statistically* true (Cho & Lazarian 2003).

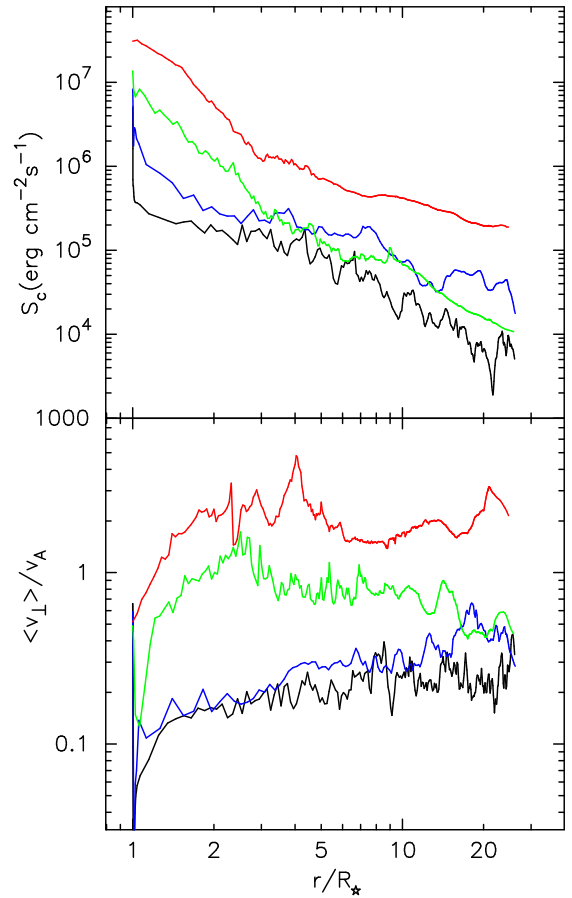


FIG. 13.— Properties of Alfvén waves in the $1 M_\odot$ stars (Models I - IV). The top panel exhibits the adiabatic constant, \mathcal{S}_c , and the bottom panel shows the nonlinearity, $\langle v_\perp \rangle / v_A$. The black, blue, green, and red lines are the results of Models I, II, III, and IV, respectively,

The process discussed here is the parametric decay instability of Alfvén waves due to three-wave (outgoing Alfvén, incoming Alfvén, and outgoing slow waves) interactions (Goldstein 1978; Terasawa et al. 1986). The decay instability is not generally efficient in the homogeneous background since it is a nonlinear mechanism. Therefore, it has not been considered as a major process of the acceleration of the solar and stellar winds. However, the density gradient of the background plasma totally changes the situation. The amplitude, v_\perp , of Alfvén waves is inevitably amplified with the decreasing density to conserve S . On the other hand, the Alfvén speed, $v_A (\propto B/\sqrt{\rho})$, does not increase so much because the decrease of B_r (flux tube expansion) compensates the decrease of ρ . As a result, the nonlinearity ($\langle v_\perp \rangle / v_A$) increases as the Alfvén waves travel upwardly (see Figure 13), which leads to efficient dissipation.

Figure 13 compares the dissipation of the Alfvén waves in the four Models of the $1 M_\odot$ stars. In the upper panel \mathcal{S}_c 's are compared, and in the lower panel nonlinearities, $\langle v_\perp \rangle / v_A$, are shown, where $\langle v_\perp \rangle = \sqrt{\langle v_\perp^2 \rangle}$. The figure shows that the wave energies drastically attenuate just above the surfaces in higher gravity stars because of the reflection in the chromospheres. In these stars the densities decrease more rapidly in the inner chromospheres,

leading to the increases of v_A 's. Then, the wavelength of the Alfvén wave with the typical frequency (e.g. several min. in Model I) becomes longer than $H_p \propto 1/g$ which itself is substantially smaller for larger g . This enhances the reflection as explained above.

Furthermore, in stronger gravity stars, the chromospheres are geometrically thin ($r - R_\star \ll R_\star$). Otherwise if the chromosphere extends to $r - R_\star \gtrsim R_\star$ as in the RGB stars, a curvature effect increases H_p by r/R_\star (Equation 15), which reduces the wave reflection. This is also a reason why the reflection becomes relatively important in the higher gravity stars. Finally, only less than half of the input wave energies can go beyond the inner chromospheres in Models I - III (§3.4.3).

Let us turn to the waves in the outer regions. Wave dissipation is more rapid in lower gravity stars. This is because the densities in the atmospheres are larger in those stars due to the longer H_p and accordingly the Alfvén speeds, $\propto 1/\sqrt{\rho}$, becomes slower. In such a condition Alfvén waves more easily become nonlinear ($\langle v_\perp \rangle / v_A \gtrsim 1$ in the bottom panel of Figure 13), which enhances the wave dissipation. Then, one may expect that the wave energies are more effectively transferred to the winds in more evolved stars. However, the situation is not so simple because in these stars radiative losses become efficient due to the higher densities. We study the wind energetics to discuss these issues in the next subsection.

Before closing this subsection we would like to remark on dissipation lengths of the Alfvén waves. Since the dissipation processes of Alfvén waves are quite complicated, a simplified phenomenological approach has been often adopted to treat Alfvén waves in solar and stellar wind models (e.g. Hartmann & MacGregor 1980); an action of Alfvén waves is assumed to follow

$$S \propto \exp\left(-\frac{r - R_\star}{l}\right), \quad (19)$$

where l is a (constant) dissipation length ($= 0.1 - 10 R_\star$). We can directly estimate l from our simulations. The upper panel of Figure 13 illustrates that the decreases of S_c 's are roughly on straight lines in the $\log(r/R_\star) - \log S_c$ diagram. This means that the dissipation lengths increase on r . For example, in Model IV $l \lesssim 1 R_\star$ in $r < 3 R_\star$, but $l \approx 10 R_\star$ in $r > 10 R_\star$; the assumption of a constant dissipation length is not appropriate.

3.4.3. Energy Transfer from Alfvén Waves

A fraction of the initial wave energy is used for the acceleration of the stellar winds, while the rest of them is lost by radiation and returned back to the stellar surface by counter propagating waves. We estimate kinetic energy fluxes of the stellar winds at the outer boundaries, integrated radiative losses, and wave energy fluxes leaking inward from the stellar surfaces, respectively, in unit of erg/s :

$$\left(\rho v_r \frac{v_r^2}{2} f r^2\right)_{\text{out}}, \quad (20)$$

$$\int_{R_\star}^{r_{\text{out}}} dr r^2 f q_R, \quad (21)$$

$$\left(\rho \langle \delta v_{\perp,-}^2 \rangle v_A\right)_\star R_\star^2, \quad (22)$$

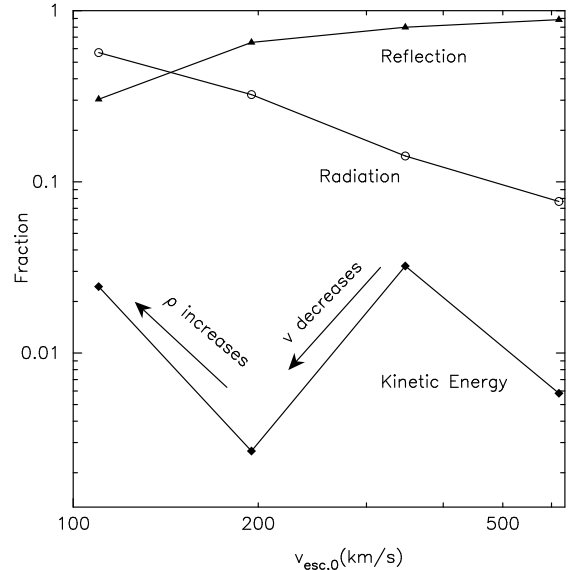


FIG. 14.— The fractions of wind kinetic energy, radiative loss, and wave energy reflected back to the surfaces of the $1 M_\odot$ stars converted from the input energy of Alfvén wave as functions of $v_{\text{esc},0}$ (km s^{-1}).

where $\delta v_{\perp,-}$ denotes amplitude of incoming Alfvén waves, and subscripts ‘ \star ’ and ‘out’ indicate that the values are evaluated at the stellar surfaces and the outer boundaries, respectively. Here, we do not discuss energy carried by waves, enthalpy, and thermal conduction away from the outer boundaries because their contributions are smaller. Figure 14 presents these energies normalized by the input energy fluxes from the surfaces,

$$\left(\rho \langle \delta v_0^2 \rangle v_A\right)_\star R_\star^2, \quad (23)$$

as functions of $v_{\text{esc},0}$.

As one can see, the fractions of the wave energies that are converted to the wind kinetic energies are small. Typically, only $\sim 1\%$ of the surface turbulent energies are transferred to the stellar winds. However, these tiny fractions are enough to keep the observed \dot{M} and $v_\infty \approx v_{20R_\star}$ of the winds from MS and RGB stars.

Most of the energy is lost by the radiation and the wave reflection. In the less evolved stars (Models I-III), the energy losses are dominated by the wave reflection as discussed in §3.4.2; the densities decrease more rapidly because of the higher gravity, and then, the wavelengths become longer than the scale heights, which results in the effective reflection via the deformation of the wave shape. The rapid decreases of the densities also make the radiative cooling less effective; it is important only in the chromospheres ($T < 10^4$ K) and low coronae where the densities are sufficiently high (volumetric radiative cooling is $\propto \rho^2$ in optically thin and $\propto \rho$ in optically thick gas). This also leads to the relative dominance of the wave reflection in the total energy loss. On the other hand, the trend of the most evolved star (Model IV) is opposite since the decrease of the density is more gradual; radiative cooling becomes relatively important first because it is efficient even in the outer region and second because the Alfvén waves do not suffer the reflection so much.

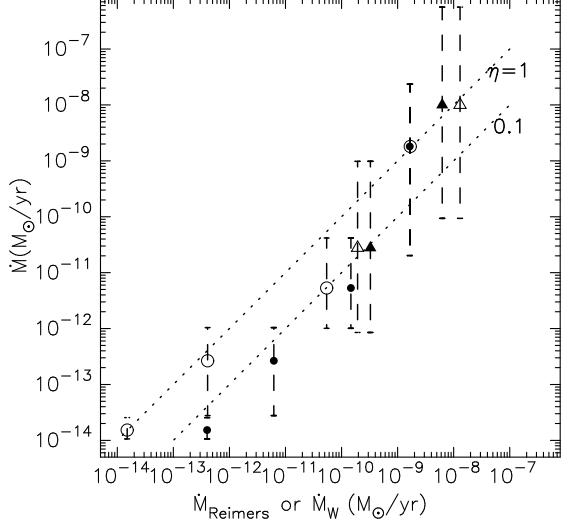


FIG. 15.— Comparison of the mass loss rates of the simulations (vertical axis) with the Reimers' relation (filled symbols; horizontal axis) and Equation (31) derived from the scaling relations of wind energetics (open symbols; horizontal axis). The circles and the triangles indicate the results of the $1M_{\odot}$ and $3M_{\odot}$ stars, respectively.

Let us turn back to the kinetic energy part. The tendency on $v_{\text{esc},0}$ is not monochromatic. From Model I (MS; $v_{\text{esc},0} = 617 \text{ km s}^{-1}$) to II (sub-giant; $v_{\text{esc},0} = 347 \text{ km s}^{-1}$), the fraction of the kinetic energy increases mainly because the mass flux, ρv_r , increases. However, the fraction drops almost by one order of magnitude from Models II to III ($v_{\text{esc},0} = 195 \text{ km s}^{-1}$). This is because of the drastic decrease of the wind speed (Figure 4). Although the density increases from Models II to III, the effect of the velocity dominates since the kinetic energy flux is proportional to ρv_r^3 . From Models III to IV ($v_{\text{esc},0} = 110 \text{ km s}^{-1}$), the decrease of v_r is small, and the fraction of the kinetic energy again increases simply by the increase of the density.

3.4.4. Mass Loss Rate

The bottom panel of Figure 4 shows the mass loss rate of the $1M_{\odot}$ star rapidly increases by ~ 5 orders of magnitude from MS to RGB phases. However, the increase of \dot{M} is continuous, which is in contrast to the velocity and temperature showing the gaps between the sub-giant and RGB stars. This is because the density in the wind drastically rises during this phase, which compensate the rapid decrease of the wind speed.

Since our simulations adopt a *forward* approach, \dot{M} is not an input parameter but an output directly determined from the simulations. Therefore, it is straightforward to study how \dot{M} evolves with the stellar evolution from the wind energetics. We begin by comparing our results with the empirical relation by Reimers (1975):

$$\dot{M}_{\text{Reimers}} = 4 \times 10^{-13} \eta_{\text{R}} \frac{(L_{\star}/L_{\odot})(R_{\star}/R_{\odot})}{(M_{\star}/M_{\odot})} M_{\odot}/\text{yr}, \quad (24)$$

where η_{R} is a proportional coefficient of an order of unity. This is based on a dimensional analysis of stellar wind energetics. The filled symbols in Figure 15 compares the obtained \dot{M} with the \dot{M}_{Reimers} for $\eta_{\text{R}} = 1$. The

comparison indicates that the Reimers' relation roughly gives reasonable estimates. However, smaller $\eta_{\text{R}} (\lesssim 0.1)$ seems to be systematically favored in the higher gravity stars. To search a better relation, we investigate the mechanism that controls \dot{M} from the energetics of our Alfvén-wave driven wind simulations.

In the wave-driven winds, the radiation part (L_{\star}) should be replaced by wave energy in Equation (24). In an open flux tube, a fraction, ϵ , of the initial energy flux of input Alfvén wave is transferred to the stellar wind where ϵ is exactly what has been derived in §3.4.3 (Figure 14). This can be written as

$$\epsilon R_{\star}^2 F_{\text{w},\star} = r^2 f \rho v_r \frac{v_r^2}{2}, \quad (25)$$

where $F_{\text{w},\text{star}} = \rho_0 \langle \delta v_0^2 \rangle v_{\text{A}}$ is wave energy flux. The left-hand side is evaluated at the surface and the right-hand side is at a sufficiently distant location at which $f = f_{\text{tot}}$ and $v \approx v_{\infty}$. Multiplied by 4π , a transformation of Equation (25) gives

$$\epsilon L_{\text{w}} = \dot{M} \frac{v_{\infty}^2}{2}, \quad (26)$$

where $L_{\text{w}} = 4\pi R_{\star}^2 F_{\text{w}}/f_{\text{tot}}$ is wave luminosity and $\dot{M} = 4\pi \rho v_{\infty} r^2$. Here $F_{\text{w}}/f_{\text{tot}}$ is used instead of F_{w} because the fraction of the area occupied by open field regions at the surface is $1/f_{\text{tot}}$. Then, an equation that determines \dot{M} becomes

$$\dot{M}_{\text{w}} = 2\epsilon \frac{L_{\text{w}}}{v_{\infty}^2} = \left(2\epsilon \frac{v_{\text{esc},0}^2 L_{\text{w}}}{v_{\infty}^2 L_{\star}} \right) \frac{L_{\star}}{v_{\text{esc},0}^2} = \left(\epsilon \frac{v_{\text{esc},0}^2 L_{\text{w}}}{v_{\infty}^2 L_{\star}} \right) \frac{L_{\star} R_{\star}}{GM_{\star}}, \quad (27)$$

where we add subscript 'w' to distinguish from \dot{M}_{Reimers} and the simulated \dot{M} . Although ϵ varies on $v_{\text{esc},0}$, we have almost constant

$$\epsilon v_{\text{esc},0}^2 / v_{\infty}^2 \approx 0.02, \quad (28)$$

because $v_{\infty}^2 / v_{\text{esc},0}^2$ is positively correlated with ϵ as shown in Figure 14.

As for the wave luminosity, we can use the scaling relations of Equations (8) and (10), and then,

$$\begin{aligned} \frac{L_{\text{w}}}{L_{\star}} &= \frac{F_{\text{w}}/f_{\text{tot}}}{\sigma T_{\text{eff}}^4} = \frac{(B_{r,0}/f_{\text{tot}}) \sqrt{\rho_0} \langle \delta v_0^2 \rangle}{\sqrt{4\pi\sigma} T_{\text{eff}}^4} \\ &= 1.4 \times 10^{-5} \frac{(T_{\text{eff}}/T_{\text{eff},\odot})^9}{(g/g_{\odot})} \end{aligned} \quad (29)$$

where σ is the Stephan Boltzmann constant, subscript, \odot , denotes the solar values, and we are using the same $B_{r,0}/f_{\text{tot}} (= 1 \text{ G})$ in all the Models.

Substituting Equations (28) and (29) into Equation (27), we finally have

$$\dot{M}_{\text{w}} = 1.7 \times 10^{-14} \eta_{\text{w}} \frac{(L_{\star}/L_{\odot})(R_{\star}/R_{\odot}) (T_{\text{eff}}/T_{\text{eff},\odot})^9}{M_{\star}/M_{\odot} g/g_{\odot}} \quad (30)$$

$$= 1.7 \times 10^{-14} \eta_{\text{w}} \frac{(L_{\star}/L_{\odot})(R_{\star}/R_{\odot})^3 (T_{\text{eff}}/T_{\text{eff},\odot})^9}{(M_{\star}/M_{\odot})^2} \quad (31)$$

in $M_{\odot}\text{yr}^{-1}$, where we leave a degree of freedom in $\eta_{\text{w}} (\approx 1)$, similarly to the Reimers' relation (Equation 24) since

ϵ is not a constant. Note that the dependences of g and T_{eff} in Equation (30) are from the dependences of the energy flux of the generated sound waves by Renzini et al. (1977) (Equation 9); if we used other results by *e.g.* Stein (1967); Bohn (1984), which give slightly different dependences, the scaling relations of \dot{M}_w would be also slightly different. \dot{M}_w does not have dependence on the properties of magnetic fields since we assume a constant $B_{r,0}/f_{\text{tot}} (= 1 \text{ G})$ in Equation (29). In more realistic situations, however, $B_{r,0}/f_{\text{tot}}$ would show star-to-star variation, and \dot{M}_w would have dependence on the magnetic fields.

The open symbols in Figure 15 compares the simulated \dot{M} and \dot{M}_w . One can see that most of the data points are distributed near $\eta_w = 1$. While the Reimers' formula, mainly targeting more luminous red giants, does not give good \dot{M} estimates for the less evolved stars (filled symbol; Equation 24), our scaling gives a better explanation to these stars. Then, the scaling of Equation (31) can connect the mass loss rate of less evolved stars to that of more evolved ones that can be handled by the Reimers' formula.

Schröder & Cuntz (2005) also proposed a formula of mass loss rates of wave-drive winds, focusing on more evolved stars. In their formula, additional dependences on g and T_{eff} also appear, while they are different from ours.

4. DISCUSSION

4.1. Magnetic Fields

When performing the simulations, we have to set up in advance the surface fluctuations and the magnetic flux tubes. While we can reasonably estimate the amplitude and period (spectrum) of the surface fluctuations from the conditions of the convection zones (§2.3), there are large uncertainties in the properties of the magnetic fields.

We only consider the open magnetic field regions because our aim is to study the stellar winds. We assume the same magnetic field strength ($B_{r,0} = 240 \text{ G}$) at the surface and expansion factor ($f_{\text{tot}} = 240$) in the different stars. Although it is unclear how in reality the open magnetic flux tubes are, we had better consider effects of different flux tubes (see Falceta-Conçalves, Vidotto, & Janenco-Pereira (2006) for configurations of flux tubes).

We have actually studied the effects of the strength and configuration of magnetic flux tubes on the solar wind by both numerical simulations (SI06) and analytical method (Suzuki 2006). We showed that $B_{r,0}/f_{\text{tot}}$ is a more important parameter in controlling solar wind properties than individual $B_{r,0}$ and f_{tot} , if nonlinear Alfvén waves dominantly work in the acceleration. This is also consistent with recent observation by Kojima et al. (2005). For example, flux tubes with different $B_{r,0}$ and f_{tot} but the same ratio $B_{r,0}/f_{\text{tot}}$ give similar wind properties if the photospheric amplitudes are the same. An input energy flux is $\sim \rho \langle \delta v_0 \rangle^2 v_{A,0} \propto B_{r,0}$ at the surface, and it is diluted according to $1/f_{r,0}^2$ in an expanding flux tube. The acceleration of the stellar wind mainly occurs in the outer region where the super-radial expansion of the flux tube already finishes. Therefore, $B_{r,0}/f_{\text{tot}}$, which is pro-

portional to S_c (\approx energy flux) of the input Alfvén wave measured at the outer region, becomes an important control parameter in the Alfvén wave-driven wind. Moreover, a mass flux, *i.e.* \dot{M} , is determined almost solely by $\langle \delta v_0 \rangle^2$, and very weakly dependent on $B_{r,0}/f_{\text{tot}}$ (SI06). Then, $B_{r,0}/f_{\text{tot}}$ plays a role only in tuning the terminal velocity of the solar wind.

This argument is directly applicable to red giant winds. \dot{M} 's of the stellar winds (the top panel of Figure 4) are determined with little uncertainty since they are mainly determined by $\langle \delta v_0 \rangle^2$ of the surface convections. However, when we discuss the wind terminal speeds, $B_{r,0}/f_{\text{tot}}$ needs to be taken carefully; wind speed becomes faster in a flux tube with larger $B_{r,0}/f_{\text{tot}}$.

$B_{r,0}/f_{\text{tot}} (= 240/240 = 1 \text{ G})$ corresponds to the total magnetic flux over the whole open field regions divided by the entire stellar surface. To discuss the average field strength we have to take into account closed regions, which occupy a sizable fraction of the surface. If 10% of the surface is occupied by open field regions, the average strength becomes 10 times, namely 10G. This value is quite reasonable from an energetics point of view. The magnetic energy density at the surface is $B_{r,0}^2/8\pi \simeq 4 \text{ erg cm}^{-3}$, which is considerably smaller than the kinetic energy of the surface turbulence, $\rho \langle \delta v_0^2 \rangle \sim 10^3 - 10^4 \text{ erg cm}^{-3}$, of the simulated stars. It is sufficient only if ~ 0.1 % of the turbulent energy is converted to the magnetic energy by motions of charged particles (*i.e.* current) in the surface convection.

Related to this, Rosner et al. (1991, 1995) tried to interpret the DL by the change of magnetic topologies. The stellar rotation becomes slow with the evolution so that the generation of magnetic fields by large-scale dynamo is switched-off. Magnetic fields are generated only by (small-scale) turbulent convection in the surface layers in evolved stars. As a result, closed fields, which have dominantly covered the surface in unevolved stars, become open in evolved stars redward of the DL. Therefore, hot plasma, which has been well confined by closed loops, would flow out.

If this scenario is correct⁵, surface field strength, $B_{r,0}$, becomes smaller in evolved stars. However, we expect that the field strength in the outer regions ($\propto B_{r,0}/f_{\text{tot}}$) is less affected, because an decrease of $B_{r,0}$ firstly reduces a fraction of closed structures rather than strength of open fields in the outer region; even if $B_{r,0}$ decreases, B_0/f_{tot} stays more or less constant before all the field lines become open. Because $B_{r,0}/f_{\text{tot}}$ is more important than $B_{r,0}$ as stated above, we anticipate that our results of the stellar winds are affected little even if the magnetic field topologies change with the stellar evolution.

4.2. Previous Wind Calculations

Hartmann & MacGregor (1980) investigated stellar winds from late-type stars with explicitly taking into account the effects of Alfvén waves. They calculated several stars with different wave energies and dissipation param-

⁵ It should be noted that Ayres, Brown, & Harper (2003) recently proposed a different scenario for the DL: even though closed loops, which are sources of X-rays, are distributed in stars redward of the DL, these X-rays are obscured by larger column density of above chromospheric material. This density effect is a reasonable explanation of the DL.

eters under the steady-state condition from assumed inner boundaries. They concluded that the dissipation of Alfvén waves resulted in coronal heating in higher gravity stars (MS and sub-giant) and mass loss in lower gravity stars (RGB). Our analysis of the time-average wind structures basically confirm this tendency, whereas our simulations have revealed the various important time-dependent aspects (§3.2).

Most of previous works claim that it is difficult to accelerate slow and dense red giant winds by Alfvén waves (Holzer et al. 1983; Charbonneau & MacGregor 1995)⁶ The main problem is that a sizable amount of the input wave energy remains in the supersonic region, which leads to faster wind. There is also a similar problem in the concept of a supersonic transition locus, which Mullan (1978) introduced to explain the onset of massive wind. The main difference of our results from the previous works is that the large subsonic regions are formed in our simulations due to the nearly static regions above the surfaces. Therefore, most of the input Alfvén wave energies are deposited in the subsonic regions, which results in the slow winds, although the dissipation is not much faster than in the previous model calculations.

We speculate that our dynamical wind solutions correspond to “inner solutions” introduced by Holzer et al. (1983). They pointed out that there are two transonic solutions in some cases; one is the inner solution in which the wind is accelerated very gradually and the wind speed is slower, although they mainly studied the other one, the outer solution, in which the acceleration starts just above the surface. Our dynamical simulations automatically select stable transonic wind solutions. Then, our results might show that the inner solution is the stable branch of Alfvén wave-driven winds.

We would like to remark on an issue of time-dependent winds. Our simulations show that some portions of the RGB atmospheres transiently accrete ($v_r < 0$), which lasts longer than the assumed longest wave periods (*e.g.* see the dashed line in the top panel of Figure 5). This phenomenon may be an example of the hysteresis transition between subsonic accretion and supersonic wind discovered by Velli (1994); Del Zanna, Velli, & Londrillo (1998).

4.3. Limitations

Here we discuss processes and effects which need to be studied in more detailed calculations.

4.3.1. Heating of Low Chromosphere: Sound Waves?

We do not input longitudinal fluctuations at the photospheres, which would directly drive sound waves, because they do not contribute to the heating and acceleration of the stellar winds (*e.g.* Judge & Carpenter 1998) (In our simulations sound waves are generated from Alfvén waves in the upper regions; §3.4.2). However, the sound waves directly from the surface might be important in the heating of low chromosphere (*e.g.* Carlsson & Stein 1997). We switch off the radiative cooling in the inner regions if $T < 3000$ K and $\rho > 5 \times 10^{-17}$ g cm⁻³ by the technical reason (§2.2). By taking into account the longitudinal perturbations at the photospheres, we may carry out a

⁶ Although these works focus on more massive RGB stars than ours, the result will not change if less massive stars are considered.

more self-consistent treatment of the low chromospheres without switching off the radiative cooling artificially.

4.3.2. Multi-dimensional Effects - Wave Generation-

In our simulations we only consider the wave generation at the photospheres in the 1D flux tubes. However, interactions between flux tubes may be important in generation of waves, though 2D or 3D modeling is required to study such processes. For example, reconnection events between closed loops could be sources of small flare-like events, and these events probably excite compressive waves at locations above the photosphere (Sturrock 1999).

The magnetic reconnection between a closed loop and an open field line also possibly excites Alfvén waves traveling upwardly (Miyagoshi et al. 2004). These waves would also play a role in the acceleration of red giant winds. Further detailed analysis is necessary to estimate how such waves produced by activities involving closed loops are important with respect to the energetics.

4.3.3. Multi-dimensional Effects - Wave Propagation-

We treat the propagation of Alfvén waves in the 1D flux tubes. In other words, Alfvén waves are assumed to travel in the same way in neighboring flux tubes. However, if Alfvén speeds are slightly different in neighboring field lines, the waves become out of phase even if they are generated in the same way at the surface. Then, these Alfvén waves dissipate by phase mixing through resistivity and viscosity (Heyvaerts & Priest 1983).

Alfvén waves in stellar winds become more or less turbulent-like. Then, Alfvénic turbulence cascades to higher frequency in the transverse direction with respect to underlying magnetic fields (Goldreich & Sridhar 1995). Therefore, Alfvén waves might dissipate by different channels in more realistic 3D calculations, while in our 1D simulations the Alfvén waves dissipate mainly through the decay instability (§3.4.2).

4.3.4. Collisionless Effects

We assume the MHD approximation, namely a mean free path with respect to Coulomb collisions, $l_{\text{mfp}} = 9.38 \times 10^7$ cm $\frac{(T/10^6 \text{ K})^2}{n/10^8 \text{ cm}^{-3}}$, is smaller than a typical scale. Here, we can take the minimum wavelength, $\lambda_{\text{min}} \simeq v_A \tau_{\text{min}}$, of the Alfvén waves as a typical scale, hence,

$$\lambda_{\text{min}} > l_{\text{mfp}} \quad (32)$$

is the requirement for the MHD condition. Otherwise we have to consider collisionless effects of plasma. This condition breaks in $r \gtrsim 2 R_\star$ of the MS star (Model I) and in $\gtrsim 5 R_\star$ of the sub-giant star (Model II), while in the RGB stars (Models III - VI) it holds in the entire simulation regions because the densities are high and the temperatures are low.

In the collisionless regime, compressive (slow/fast MHD) waves suffer collisionless damping (Barnes 1966; Suzuki et al. 2006). Then, the dissipation rate of the slow MHD waves, which are nonlinearly generated from the Alfvén waves, may be changed. This might further modify the mode conversion rate from the Alfvén waves. Then, the dissipation of the Alfvén waves might be indirectly affected in Models I and II.

4.3.5. Atoms, Molecules, and Dusts

In the RGB atmospheres, the temperatures sometimes become $10^3 - 10^4$ K as shown in the snap-shot results (Figures 5 & 9). Although even in such low temperatures a fraction of the gas is expected to be ionized by the UV/X-ray emissions from hot bubbles, a sizable amount of neutral atoms remain, or even molecules can also exist if $T \lesssim 3000$ K (Tsuji 1973). The snap-shot results also show that the temperatures partly decreases further to ~ 1000 K, and in such circumstances dusts are also formed.

The existence of atoms and molecules indicate that the gas is not fully ionized but partially ionized. The MHD approximation implicitly assumes that the coupling between ions and neutrals is sufficient so that the gas can be treated as one fluid. Otherwise, the friction between these two components plays a role in the dissipation of Alfvén waves. We can check the condition of ion-neutral coupling by comparing wave frequency and a ion-neutral collision rate (Draine, Roberge, & Dalgarno 1983). We have found that the coupling is sufficient with respect to the low-frequency waves we are dealing with; we do not have to worry about the effect of weakly ionized gas. However, if high frequency Alfvén waves are generated by turbulent cascade, these waves dissipate by the ion-neutral damping more effectively than in fully-ionized gas (Holzer et al. 1983).

Molecules can be used as diagnostics to understand physical conditions of RGB star atmospheres. Observations of CO show that quasi-static cool ($T \sim 1000 - 2000$ K) regions containing molecules are in the atmospheres of RGB stars, typically at $\sim 2R_*$ (Tsuji 1988; Tsuji et al. 1997). Our simulations of the RGB stars also show the quasi-static regions in the atmospheres and the temperatures partly becomes low enough to form molecules. The cooling by molecules drive thermal instability at $T = 2000 - 3500$ K (Muchmore, Nuth, & Stencel 1987), similarly to the ions in $T \gtrsim 10^5$ K. This will be important in controlling thermal properties of the atmospheres and winds of RGB stars.

Radiation pressure on dusts is not efficient in driving winds of RGB stars (Judge & Stencel 1991; Vidotto & Janenco-Pereira 2006), although it could be important in asymptotic giant branch stars. However, Alfvén waves may dissipate by the cyclotron resonance with charged dusts (Vidotto & Janenco-Pereira 2006), which might also give a correction to the dissipation of the Alfvén waves. To study this effect, we have to carefully consider the formation processes of dusts in intermittently existing cool ($T \sim 1000$ K) gas.

5. SUMMARY

We have studied the winds of the intermediate and low mass RGB stars near the DL, by comparing with the coronal winds from the MS and SB stars. These stars all have the surface convective layers, which play a major role in driving the stellar winds as well as the UV/X-ray activities because other mechanisms such as centrifugal force and radiation pressure are insufficient. The surface turbulences excite various types of waves, among which the Alfvén wave travels a longer distance and contribute to not only the atmospheric heating near the surface but the wind acceleration in \gtrsim several R_* .

We have, for the first time, successfully carried out the

time-dependent MHD simulations of the red giant winds in the open magnetic field regions from the photospheres to the sufficiently distant locations ($\approx 25 R_*$). We inject the fluctuations from the photospheres, of which the amplitudes and spectra are estimated from the properties of the surface convection. We have determined the velocities, densities, and temperatures of the stellar winds in a self-consistent manner by taking into account the radiative cooling and thermal conduction; the propagation and dissipation of the MHD waves are automatically treated, and the subsequent heating and acceleration of the gas are also self-consistently handled by the jump conditions of the MHD shocks, using the nonlinear MHD Godunov-MOCCT algorithm.

The stellar winds are driven by the nonlinear dissipation of the Alfvén waves through the conversion to compressive waves, whereas other dissipation processes might become important when performing 3D modeling/simulations. The energy fraction that is transferred to the stellar wind against the initial wave energy is quite small, $\sim 1\%$, and the rest of the energy is lost by the wave reflection (less evolved stars) and radiation (more evolved stars). However, this tiny fraction is enough to explain the observed stellar winds from MS and RGB stars.

When the stars evolve to slightly blueward positions of the DL, the steady hot coronae with temperature, $T \gtrsim 10^6$ K, disappear. In the atmospheres and winds of the RGB stars magnetized hot bubbles and cool chromospheric gas co-exist. The hot bubbles are created in fast MHD shocks and supported by the magnetic pressure. Therefore, the densities of the bubbles can be kept low. The radiative cooling is reduced to balance with the heating so that the bubbles survive much longer than the cooling timescale.

The red giant winds are structured with many bubbles and blobs, and the mass loss rate and wind speed show large time-variations. The hot bubbles possibly become sources of EUV and soft X-ray emissions of hybrid stars, whereas the cool chromospheric wind might absorb the emissions. The temperatures of the hot bubbles become lower in more evolved and less massive stars, which is consistent with the trends inferred from the observations of hybrid stars.

The wind velocities also drop to $10-100$ km s $^{-1}$ in the RGB stars, which are much slower than the escape speeds at the stellar surfaces. This is mainly because the static atmospheres are formed above the photospheres and the stellar winds are practically accelerated from several stellar radii. The terminal velocities are regulated by the escape speeds there, and the slower winds can escape.

We have finally derived a relation (Equation 31) that determines the mass loss rates of MS to RGB stars from the energetics of the simulated wave-drive winds. This has a different dependence on the stellar parameters from the well known Reimers' formula which mainly focuses on more evolved giants. The derived relation gives a better explanation of \dot{M} of less luminous stars and can be used complementarily to the Reimers' formula.

The author thanks Profs. T. Tsuji, H. Shibahashi, H. Ando, T. Watanabe, and S. Inutsuka for many fruitful discussions. The author also thanks the referee for many constructive comments. This work is supported in part by a Grant-in-Aid for Scientific Research (18840009)

from the Ministry of Education, Culture, Sports, Science, and Technology of Japan.

REFERENCES

- Anderson, C. S. & Athay, R. G. 1989, *ApJ*, 336, 1089
 Ayres, T. R. 2005, *ApJ*, 618, 493
 Ayres, T. R., Brown, A., & Harper, G. M., 2003, *ApJ*, 598, 610
 Ayres, T., Linsky, J. L., Vaiana, G. S., Golub, L., & Rosner, R. 1981, *ApJ*, 250, 293
 Ayres, T. R., Simon, T., Stern, R. A., Drake, S. A., Wood, B. E., & Brown, A. 1998 *ApJ*, 496, 428
 Barnes, A. 1966, *Phys. Fluid*, 9, 1483
 Bohn, H. U. 1984, *A&A*, 136, 338
 Carlsson, M. & Stein, R. F. 1997, *ApJ*, 481, 500
 Charbonneau, P. & MacGregor, K. B. 1995, *ApJ*, 454, 901
 Cho, J. & Lazarian, A. (2003), *MNRAS*, 345, 325
 de Loore, C. 1970, *Ap&SS*, 6, 60
 Del Zanna, L., Velli, M., & Londrillo, P. 1998, *A&A*, 330, L13
 Draine, B. T., Roberge, W. G., & Dalgarno, A. 1983, *ApJ*, 264, 485
 Dupree, A. K. 1986, *ARA&A*, 24, 377
 Falceta-Conçalves, D., Vidotto, A. A., & Janenco-Pereira, V. 2006, *MNRAS*, 368, 1145
 Girardi, L., Bressan, A., Bertelli, G., & Chiosi, C. 2000, *A&AS*, 141, 371
 Goldreich, P. & Sridhar, S. 1995, *ApJ*, 438, 763
 Goldstein, M. L. 1978 *ApJ*, 219, 700
 Gray, D. F. 1992, "The observation and analysis of stellar photospheres", *Cambridge*
 Hammer, R. 1982, *ApJ*, 259, 767
 Harper, G. M., Wood, B. E., Linsky, J. L., Bennett, P. D., Ayres, T. R., & Brown, A. 1995, *ApJ*, 452, 407
 Hartmann, L., Dupree, A. K., & Raymond, J. C. 1980, *ApJ*, 236, L143
 Hartmann, L. & MacGregor, K. B. 1980, *ApJ*, 242, 260
 Heyvaerts, J. & Priest, E. R. 1983, *A&A*, 117, 220
 Holzer, T., E., Flå, T., & Leer, E. 1983, *ApJ*, 808
 Holweger, H., Gehlsen, M., & Ruland, F. 1978, *A&A*, 70, 537
 Hünsch, M. & Schröder, K.-P. 1996, *A&A*, 309, L51
 Jacques, S. A. 1977, *ApJ*, 215, 942
 Judge, P. G. & Carpenter, K. G. 1998, *ApJ*, 494, 828
 Judge, P. G. & Stencel, R. E. 1991, *ApJ*, 371, 357
 Kim, J. & Ryu, D. 2005, *ApJ*, 630, L45
 Kojima, M., K. Fujiki, M. Hirano, M. Tokumaru, T. Ohmi, and K. Hakamada, 2005, "The Sun and the heliosphere as an Integrated System", G. Poletto and S. T. Suess, Eds. Kluwer Academic Publishers, 147
 Kopp, R. A. & Holzer, T. E. 1976, *Sol. Phys.*, 49, 43
 Koyama & Inutsuka 2002, *ApJ*, 564, L97
 Kudoh, T. & Shibata, K. 1999, *ApJ*, 514, 493
 Landini, M. & Monsignori-Fossi, B. C. 1990, *A&AS*, 82, 229
 Lamers, H. J. G. L. M. & Cassinelli, J. P. 1999, 'Introduction to Stellar Wind', Cambridge
 Lighthill, M. J. 1952, *Proc. Roy. Soc.*, A211, 564
 Linsky, J. L. & Haisch, B. M. 1979, *ApJ*, 229, L27
 Miyagoshi, T., Yokoyama, T., Isobe, H., & Shibata, K. 2004, *ASP Conf. Series* (5th Solar-B Science Meeting), 325, 69
 Moore, R. L., Suess, S. T., Musielak, Z. E., & An, A.-H. 1991, *ApJ*, 378, 347
 Moriyasu, S., Kudoh, T., Yokoyama, T., & Shibata, K. 2004, *ApJ*, 601, L107
 Muchmore, D. O., Nuth, J. A. III, & Stencel, R. E. 1987, *ApJ*, 315, L141
 Mullan, D. J. 1978, *ApJ*, 226, 151
 Reimers, D. 1975, *Mem. Soc. Roy. Sci. Liège*, 6e Ser. 8, 368
 Renzini, A., Cacciari, C., Ulmschneider, P., & Schmitz, F. 1977, *A&A*, 61, 39
 Rosner, R., An, C.-H., Musielak, Z. E., Moore, R. L., & Suess, S. T. 1991, *ApJ*, 372, L91
 Rosner, R., Musielak, Z. E., Cattaneo, F., Moore, R. L., & Suess, S. T. 1995, *ApJ*, 442, L25
 Sakurai, T., Ichimoto, K., Raju, K. P., & Singh, J. *Sol. Phys.*, 209, 265
 Schröder, K.-P. & Cuntz, M. 2005, *ApJ*, 630, L73
 Shibahashi, H. 2005, *J. Astrophys. Astr.* 26, 139
 Stein, R. F. 1967, *Sol. Phys.* 2, 385
 Stein, R. F., Georgobiani, D., Trampedach, R., Ludwig, H.-G., & Nortlund, Å. 2004, *Sol. Phys.*, 220, 229
 Stencel, R. E. & Mullan, D. J. 1980, *ApJ*, 238, 221
 Sturrock, P. A. 1999, *ApJ*, 521, 451
 Suzuki, T. K. 2002, *ApJ*, 578, 598
 Suzuki, T. K. 2004, *MNRAS*, 349, 1227
 Suzuki, T., K. 2006, *ApJ*, 640, L75
 Suzuki & Inutsuka 2005, *ApJ*, 632, L49 (SI05)
 Suzuki & Inutsuka 2006, *J. Geophys. Res.*, 111, A6, A06101 (SI06)
 Suzuki, T. K., Yan, H., Lazarian, A., Cassinelli, J. P. 2006, *ApJ*, 640, 1005
 Terasawa, T., Hoshino, M., Sakai, J. I., & Hada, T. 1986, *J. Geophys. Res.*, 91, 4171
 Tsuji, T. 1973, *A&A*, 23, 411
 Tsuji, T. 1988, *A&A*, 197, 185
 Tsuji, T., Ohnaka, K., Aoki, W., & Yamamura, I. 1997, *A&A*, 320, L1
 Tu, C.-Y., Zhou, C., Marsch, E., Xia, L.-D., Zhao, L., Wang, J.-X., & Wilhelm, K. 2005, *Science*, 308, 519
 Velli, M. 1994, *ApJ*, 432, L55
 Vidotto, A. A. & Janenco-Pereira, V. 2006, *ApJ*, 639, 416
 Yi, S., Demarque, P., & Kim, Y.-C. 1997, *ApJ*, 482, 677